

Peer-Reviewed Technical Communication

Characterization and System Identification of an Unmanned Amphibious Tracked Vehicle

Joseph G. Marquardt, Jose Alvarez, and Karl D. von Ellenrieder, *Member, IEEE*

Abstract—Experimental testing of an unmanned amphibious tracked vehicle on dry sand, in the surfzone and in water, has been performed to explore its maneuvering and performance characteristics for the planned future development of an automatic control system. The 2.69-m-long, 295-kg concept vehicle utilizes a small waterplane area twin hull (SWATH) configuration with integrated crawler tracks and twin propellers for propulsion. Maximum traversable incline tests on dry sand reveal that the vehicle has a drawbar pull (DP) of about 1000 N (about one third of its weight) and can operate on slopes of 15° briefly and 10° for extended periods of time. Maneuvering tests were performed on flat, dry sand, as well as into and out of a surfzone at a beach site with inclines ranging from about 3° to 6°. In each of the tests, the track forces, speed over ground, and both linear and rotational accelerations were measured. Also recorded were environmental conditions, such as wind speed, significant waveheight/period, and ground slope. The tests reveal that the vehicle has a maximum straight-line flat ground speed of about 2 m/s, a minimum flat ground turning radius of 2.4 m, an in-water minimum turning radius of 1.9 m, and a maximum straight-line waterborne speed of 1.2 m/s. It is also shown that system identification applied to the data recorded from the flat ground and waterborne maneuvering tests can be used to find a linear, parametric state-space model for the vehicle that adequately reproduces its motion. Land-to-sea transition tests in two different seas of one-third significant waveheights of 8 and 28 cm (both measured at a distance of 6 m from the mean waterline on the beach) show that the vehicle exhibits substantial track slip as it traverses into the surfzone and its weight becomes increasingly supported by the displacement of its hulls. The tractive force model developed by Wong (*Theory of Ground Vehicles*, New York, NY, USA: Wiley, 2001) is modified to account for the reduction in track-supported vehicle weight as the vehicle becomes waterborne. It is shown that this adapted model captures the main physical features of the measured track forces. The waveheights and periods recorded during surfzone transition tests are used to examine the seakeeping properties of the vehicle. It is found that the vehicle's natural frequency of roll is near the dominant wave frequencies measured. A Froude–Krylov strip theory simulation shows that the wave forces acting on the vehicle in 28-cm waves may be slightly larger than the force measured

on each track when the DUKW-Ling is crossing the transition zone between the beach and surfzone and should not be ignored in modeling and simulation studies.

Index Terms—Amphibious vehicles, system identification, unmanned vehicles.

I. INTRODUCTION

AN understanding of a vehicle's maneuverability and dynamic performance characteristics is important for the development of an automatic control system that will command its motion and can also serve as a guide for the future design of similar vehicles. An automatic controller for an amphibious vehicle must be capable of suitably performing across the diverse environments of land and sea, as well as the transition zone in-between. While gain scheduling or other methods may be used when an amphibious vehicle is either completely landborne or completely waterborne, the transition zone is the main area of uncertainty for the development of automatic controllers because the energetic and dynamic surfzone often contains breaking waves, surge, and partially liquefied terrain, which can change abruptly and can be difficult to model. A dearth of experimental data for vehicles operating in this zone further complicates their design and the development of controls-oriented models and algorithms [5], [6].

Here, in the spirit of providing new insights into the design and control of amphibious vehicles, we present a detailed characterization of the maneuvering performance of a small, tracked unmanned amphibious vehicle called the DUKW-Ling. The main scholarly outcomes of this work are an experimental characterization of the track forces acting on the vehicle as it moves from sea to land and from land to sea, and the development of a corresponding tractive force model that can be utilized for the future design and control of tracked amphibious vehicles.

The paper is organized as follows. The particulars of the vehicle, its design, and instrumentation are described in Section II. In Section III, we characterize the maneuvering performance of the vehicle when landborne and when waterborne. We develop controls-oriented state space models of the vehicle through the system identification of experimental data in Section IV. The seakeeping properties of the vehicle are explored in Section V, where we compare the normal mode frequencies of pitch, heave, and roll to measured wave data

Manuscript received October 29, 2012; revised May 03, 2013; accepted August 23, 2013. Date of publication October 17, 2013; date of current version October 09, 2014. This work was supported by the U.S. Office of Naval Research under Grant N00014-11-1-0423, managed by K. Cooper.

Associate Editor: F. Hover.

J. G. Marquardt is with the Department of Ocean & Mechanical Engineering, Florida Atlantic University, Dania Beach, FL 33004-3023 USA and also with Q Management, Gladstone, NJ 07934 USA (e-mail: joemarquar@gmail.com).

J. Alvarez and K. D. von Ellenrieder are with the Department of Ocean & Mechanical Engineering, Florida Atlantic University, Dania Beach, FL 33004-3023 USA (e-mail: jalvar36@fau.edu; ellenrie@fau.edu).

Color versions of one or more of the figures in this paper are available online at <http://ieeexplore.ieee.org>.

Digital Object Identifier 10.1109/JOE.2013.2280074

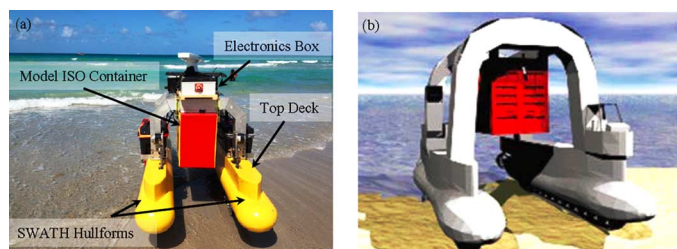


Fig. 1. (a) The DUKW-Ling unmanned amphibious vehicle. (b) The DUKW-21 amphibious ship-to-shore cargo transfer design concept [8].

at our test site. In Section VI, the experimentally measured track forces propelling the vehicle as it transitions from sea to land and from land to sea are examined. In Section VII, a Froude–Krylov analysis coupled with first principles modeling is used to estimate the effects that wave forces have on the forward speed of the vehicle as it transitions from sea to land; these estimates are shown to compare well to our experimental data. The relation between track-supported, and buoyancy-supported vehicle weight and track slip are explored. We modify the tractive force model developed by Wong [15] to account for buoyancy-supported vehicle weight and bidirectional slip (which could be caused by wave forcing) and demonstrate that it captures the main physical features experimentally observed in the transition zone. Finally, in Section VIII, some concluding remarks are given regarding the implications of our results.

II. THE DUKW-LING AMPHIBIOUS VEHICLE

A. Overview

The DUKW-Ling [Fig. 1(a)] is a 1/7th-scale model of a tracked amphibious vehicle design concept called the DUKW-21 [Fig. 1(b)], which was developed by the Center for Innovation in Ship Design at the Naval Surface Warfare Center, Carderock Division (Bethesda, MD, USA) [5], [6], [8]. The full-scale vehicle would lift and transport 6.10-m International Standards Organization (ISO) containers to offshore ships in areas where conventional methods of supply may be difficult or impractical, thereby reducing onshore footprint and logistics. The 1/7th-scale system presented here was developed as a test bed to explore the engineering challenges that might arise in the implementation of any full-scale system, as well as, to develop modeling and control techniques for tracked unmanned amphibious vehicles.

To mitigate wave-induced motion in the surfzone, the vehicle utilizes a small waterplane area twin hull (SWATH) configuration [9]. The typical SWATH hull form also possesses a relatively flat bottom (baseplane) which makes it convenient to incorporate tracks for land navigation. A propeller-based thruster is mounted at the stern of each hull; both on-land steering and on-water steering are accomplished using differential thrust. The model's principal characteristics are shown in Table I.

The 1/7th-scale model possesses a forklift-style cargo handling mechanism, shown in Fig. 2. A small winch, hydraulic linear actuators, and momentary switches are used to control the lifting and lowering of a set of arms for handling a 1/7th-scale

TABLE I
PRINCIPLE CHARACTERISTICS OF THE DUKW-LING. THE LOCATION OF THE “KEEL” IS TAKEN AS THE BOTTOM OF THE TRACKS; “W.R.T.” MEANS “WITH RESPECT TO”

Parameter	Value
Length Overall (LOA)	2.69 [m]
Length on the Waterline (LWL)	2.54 [m]
Draft (T)	0.49 [m]
Beam Overall (BOA)	1.14 [m]
Beam on the Waterline (BWL)	0.89 [m]
Depth (keel to top deck)	0.61 [m]
Area of the Waterplane (A_w)	0.89 [m ²]
Centerline-to-centerline Side Hull Separation (2p)	0.81 [m]
Length to Beam Ratio (L/B)	2.36
Displacement (Δ)	2894 [N]
Vertical center of gravity w.r.t keel (\overline{KG})	0.50[m]
Metacentric Height (\overline{GM})	0.14 [m]
Longitudinal center of gravity w.r.t bow (LCG)	1.32 [m]

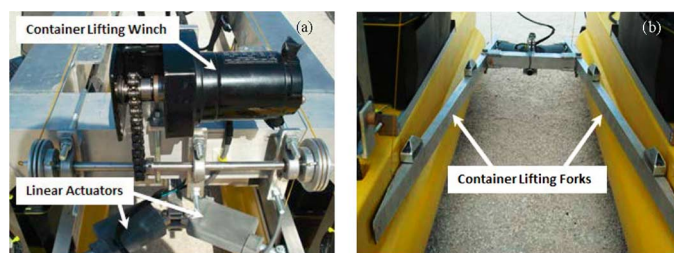


Fig. 2. ISO container lifting mechanism: (a) winch and linear actuators; and (b) lifting forks.

ISO container for transport. During testing, the forklift system secures the model ISO container.

B. Ground Propulsion System

The vehicle uses a double-ramped track configuration, which allows it to approach and depart larger obstacles than a single or no-ramp track system. For tracked vehicles, the ratio of the length of track in contact with the ground and the beam should be between 1.3 and 1.8, as lower ratios may have difficulty tracking a straight line (course keeping) and larger ones can hinder turning [7]. The DUKW-Ling has a track-length-to-beam ratio of 1.38, which was found to provide the vehicle with good maneuverability, while still having adequate course keeping [12]. The foremost ground roller mounts can be adjusted slightly in the fore–aft direction to increase the tension in the tracks [Fig. 3(c)].

Each track is constructed of an acetyl plastic conveyor belt and, as shown in Fig. 3(a), grouser were created by adding raised plastic strips to provide increased traction in sand. The bottom six wheels carry the load of the vehicle, and the front and aft sprockets keep the track in place. The front sprocket is driven by a chain and gears using an electric motor mounted on the vehicle's superstructure. The main track is shown schematically in Fig. 4, and the dimensions are listed in Table II.

To determine the correct gearing and drive motor size needed for the track system, a series of dynamometer and rolling resistance tests were conducted. Estimates of the expected rolling resistance and static friction were determined by attaching a



Fig. 3. (a) Closeup of the tracks; (b) side view of the DUKW-Ling; and (c) detail of the tracked drivetrain.

load cell to the vehicle and towing it through different terrains that the vehicle might operate in. This testing was performed across different inclines, as well as soft sand, hard packed sand, and across the water line at a beach to find the force required to move the vehicle from rest. The maximum resistance measured in these tests was used to determine suitable gearing of the motor and chain drive system; as a precaution, a 20% margin of error was added to the maximum measured resistance. A maximum rolling resistance of about 890 N was measured during tests when the vehicle was partially submerged in the surfzone. Thus, a resistance of 1068 N was used in the gearing calculations.

A four sprocket chain drive system was chosen to transfer the torque required to move the vehicle, as well as, to permit the drive motors to operate near their most efficient speed. The configuration allows for a 7:1 gear reduction, without the use of a complex worm gear. The motor sprocket has a 2.54-cm diameter while the final tread drive sprocket has a diameter of 17.27 cm. All sprockets, chain, and drivetrain components are constructed from stainless steel for corrosion resistance. It was found that sand intrusion did not significantly affect the performance of the drivetrain.

C. Waterborne Propulsion System

When waterborne, the vehicle is propelled using a pair of two-bladed, 12-V electric trolling motors. Each propulsion unit is capable of producing up to 133 N of thrust.

D. Command, Control, and Communications Electronics

For the vehicle maneuvering characterization tests, as well as for planned future automatic control development work, the sensor suite includes a Global Positioning System (GPS)-enabled inertial measurement unit (IMU), differential GPS (DGPS), tilt-compensated digital compass, depth sensor, and water sensors. The vehicle's sensors, a single-board computer (SBC) for automatic control/data acquisition, and battery power for these electronic systems are located within a waterproof electronics box (Fig. 5), which is mounted on top of the vehicle

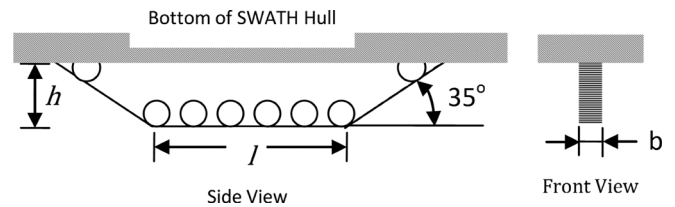


Fig. 4. Main track dimensions (also see Table II). The cross-hatched areas represent the lower portions of the SWATH hulls.

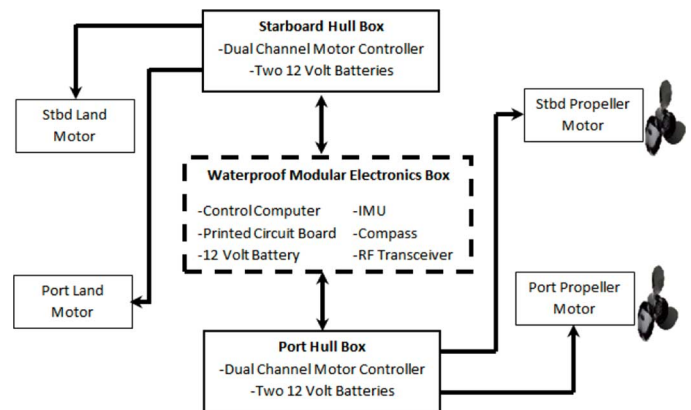


Fig. 5. Overview of vehicle electronics.

superstructure [Fig. 1(a)]. The control computer, sensors, power monitoring and conditioning electronics, and communication electronics are integrated using a custom-built printed circuit board; see Fig. 6.

There are also two motor controllers that drive the track system and propeller motors. The motor controllers and battery systems for propulsive power are located in additional waterproof housings on top of the port and starboard hulls, and are electrically isolated from the command and control power.

Wireless communications between a shore-based laptop and the vehicle are handled using either a radio-frequency (RF) transceiver or WiFi. Generally, the WiFi system has a limited range (~ 100 m). It is used for *in situ* reprogramming of the DUKW-Ling, which may require uploading large executable files. The RF transceiver has a longer range, but lower bandwidth, and so is typically used for real-time vehicle monitoring and as a secondary mode of data acquisition (in addition to onboard logging). Both wireless communication paths are open at the same time and can be used to support remote supervisory control of the vehicle.

A 12-channel servo controller is used to switch the control authority of the vehicle between a handheld remote control (RC) transmitter and onboard computer control. Thus, it is possible for a user to override onboard computer control of the DUKW-Ling and manually control the vehicle if it is not operating as expected, or in an emergency.

Water sensors are installed fore and aft to detect entry and exit from the water. These sensors consist of two short leads spaced about 6 mm apart and configured so that the sensor must be submerged in order for it to be triggered. The gap reduces the likelihood that humidity or small water droplets can falsely activate the sensors. In addition, an Airmar DT800 depth sensor is

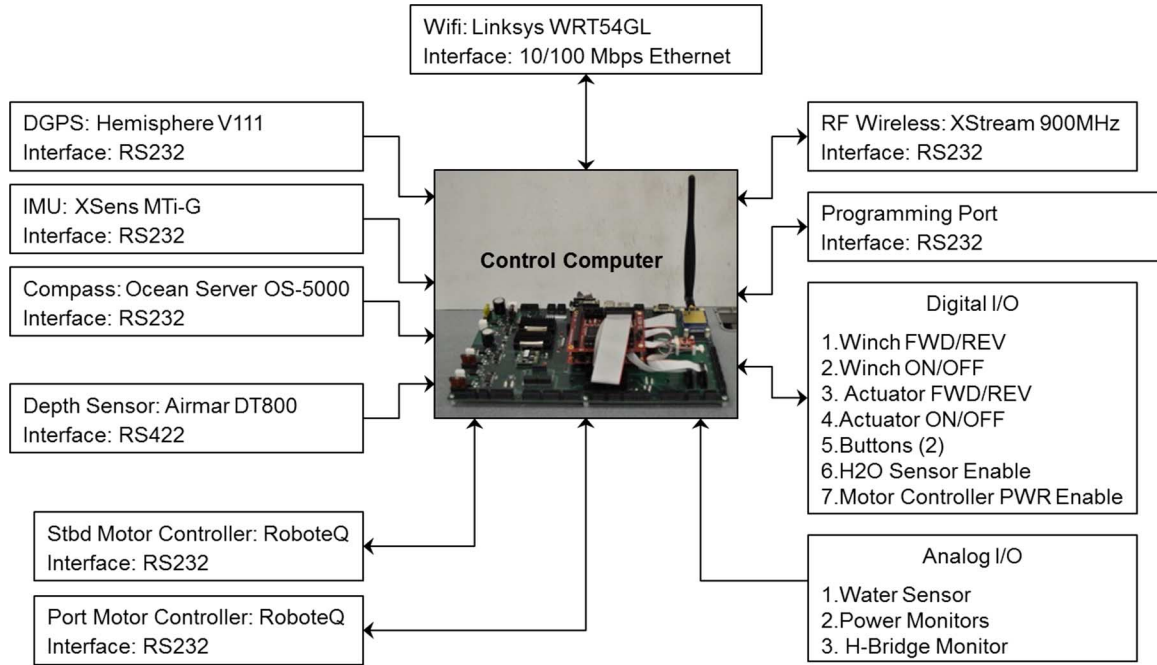


Fig. 6. Schematic of the command, control, and communication system.

TABLE II
MAIN TRACK DIMENSIONS (SEE FIG. 4)

Parameter	Value
Track length in contact with ground (l)	1.07 [m]
Track width (b)	8.26 [cm]
Ground Clearance of SWATH Hulls (h)	25.0 [cm]

mounted on the vehicle and can be used when the vehicle is operated in water deeper than about 0.5 m. Together with real-time track force measurements (see Section III-A1a), the information from these analog water sensors can be used to determine when it is appropriate to use either the tracks or the propellers for propulsion.

E. Sensor and Test Equipment Calibration

All sensors and test equipment were calibrated before testing. Estimates of the accuracy of each of the IMU's dynamic rate and acceleration channels are difficult to obtain. The IMU uses its GPS, magnetometer, and an extended Kalman filter to update the output of each channel; the accuracy of the rate and acceleration channels are a function of past motion history, GPS satellite coverage, the local variability of the Earth's magnetic field, temperature, the mounting position of the sensor within the vehicle and other parameters. An estimate of the static accuracy of the rate and acceleration channels of the unit used in the DUKW-Ling was obtained in [16] and is reprinted in Table III.

The compass was calibrated with hard and soft iron calibrations, according to the procedure provided by the manufacturer. Similarly, the dynamometer used to characterize the performance of the motors of the track drive system was also calibrated per manufacturer's instructions.

TABLE III
MEASURED STATIC ACCURACY OF DUKW-LING RATE AND ACCELERATION CHANNELS (WITHOUT GPS)

Channel	Standard Deviation
Surge [m/s^2]	0.010
Sway [m/s^2]	0.009
Heave [m/s^2]	0.009
Roll Rate [$^\circ/\text{s}$]	0.172
Pitch Rate [$^\circ/\text{s}$]	0.172
Yaw Rate [$^\circ/\text{s}$]	0.172

III. LANDBORNE AND WATERBORNE MANEUVERING CHARACTERISTICS

Maneuvering tests on land were performed on the beach in Dania Beach, FL, USA. Unless otherwise indicated, the land-based maneuvering and turning experiments reported below were conducted on dry-level sand. The waterborne maneuvering tests were performed in nearby, sheltered calm water sections of the U.S. Intracoastal Waterway.

A. Land-Based Tests

Drivetrain testing began by performing initial experiments aimed at understanding the capabilities of the model and drivetrain. The DUKW-Ling was driven by remote control in all of its different operating environments. The limitations of the vehicle, such as the maximum incline it could climb, approach and departure angles, rough estimates of its turning radius both on land and at sea, were noted so that test plan development could take these parameters into consideration. Once this initial testing was complete, more rigorous performance experiments were also conducted using open-loop computer control to collect data useful for the planned future design of a closed-loop automatic control system.

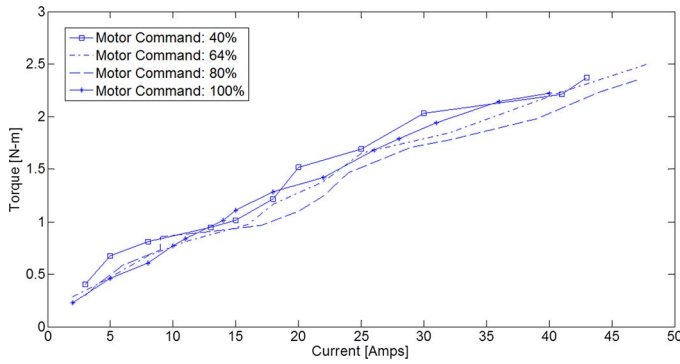


Fig. 7. Dynamometer test results: current torque relationship for different motor commands.

1) Steady-State Tests:

a) *Trackforce characterization:* A dynamometer was used to test the torque output of the electric motors that drive the tracks (Fig. 7). It was found that both motors yielded approximately the same results. Eight different speed commands, from 40% to 100% of full speed, were tested; to simplify the presentation of the data, only four of the tests are shown here. An examination of the data reveals a linear relationship between motor current and output torque across the range of commanded motor speeds.

Through knowledge of the drivetrain gear ratio, the data were used to determine an empirical relation between the current applied at each track drive motor and the corresponding force on each track

$$\text{force on track [N]} = 2.49 \times \text{motor current [A]}. \quad (1)$$

b) *Maximum traversable incline:* Concept design studies of the full-scale vehicle identified the maximum traversable incline angle as an important parameter for the development of automatic control system strategies [5], [6]. Thus, experiments were performed to measure this angle, as well as to provide information on the power draw of the motors during uphill maneuvers for planned future development of the vehicle; overloading the motors for an extended period of time could damage them. To characterize the motor loading, the vehicle was operated on different inclines to determine the current drawn by the motors. The electric motors are rated for a maximum input power of 900 W. Since they are operated at 24 V, the maximum current input should be limited to about 35 A. While this value can be exceeded for a short period of time, a higher current for an extended period could harm the motors. The ground slope over which the vehicle moves is measured by onboard sensors and could be monitored by an automatic control system to avoid motor damage due to traversing steep inclines for prolonged periods of time.

The vehicle was tested on three different sections of a beach with inclines of 11°, 14°, and 19°. During operation on these inclines, the current to the motors was measured and recorded, along with IMU data, and pitch angle. Equal motor commands of 100% of full scale to both the port and starboard track motors were used for each test. The vehicle was started at the base of each incline and was stopped when it either stalled for more

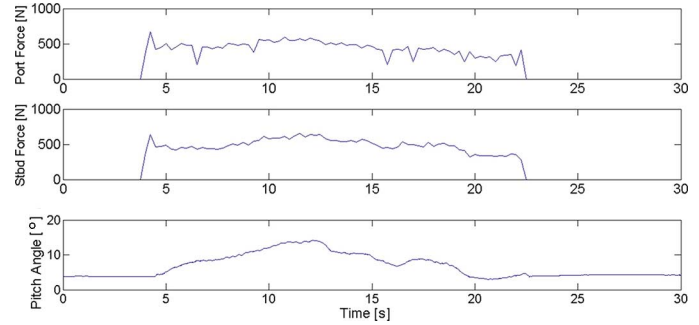


Fig. 8. Port and starboard track forces, and pitch angle versus time for incline test 1 (11° slope).

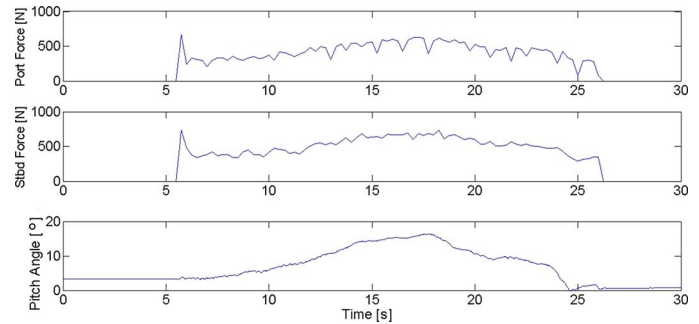


Fig. 9. Port and starboard track forces, and pitch angle versus time for incline test 2 (14° slope).

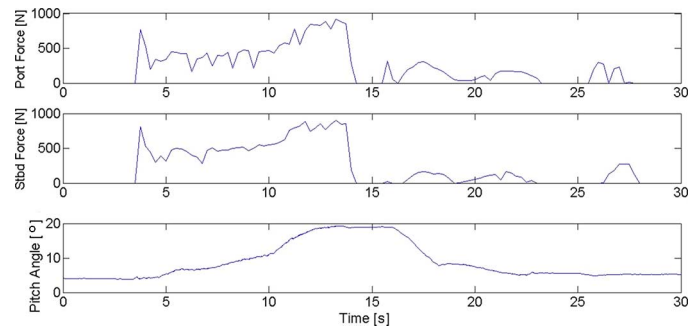


Fig. 10. Port and starboard track forces, and pitch angle versus time for incline test 3 (19° slope). This test exceeded the operating limit of the vehicle as it stalled without any track slip and was unable to traverse the incline. The test was interrupted after about 14 s to prevent damage to the track drive motors. At that time, the vehicle's open-loop controller was overridden using a handheld remote transmitter. The track forces recorded after 14 s were generated as the vehicle was manually backed down the incline.

than 10 s or was back on flat ground (Figs. 8–10). The current draw measured on each motor in incline test 3 was more than 66% larger than the desired maximum of 35 A. If the vehicle was subjected to an incline this steep for an extended period of time, motor damage would occur. The average current draw and track forces found while operating the vehicle on inclines are summarized in Table IV.

Based on the results of these tests, it is recommended that the vehicle should not be operated on inclines of more than 10° (original maximum incline design requirement) for extended periods, as the high current could damage the electric motors.

c) *Drawbar pull:* At constant speed on a level surface, the drawbar pull (DP) of a tracked vehicle is the difference between

TABLE IV
AVERAGE CURRENT AND TRACK FORCE DURING INCLINE EXPERIMENTS

	Test 1 (11° Incline)		Test 2 (14° Incline)		Test 3 (19° Incline)	
Motor	Current [Amps]	Track Force [N]	Current [Amps]	Track Force [N]	Current [Amps]	Track Force [N]
Port	35.36	288.47	39.49	322.17	54.83	447.39
Starboard	42.53	347.00	43.69	356.50	61.46	501.45

TABLE V
Turning Radii: Land-Motor Command Values Are Given as a Percentage of Full Scale

Left Turn				Right Turn			
Port %	Stbd %	Radius [m]	Speed [m/s]	Port %	Stbd %	Radius [m]	Speed [m/s]
60	84	5.34	1.3	84	60	5.57	1.3
28	44	5.24	0.4	44	28	5.45	0.4
36	60	3.69	0.7	60	36	4.15	0.7
44	84	2.44	1.1	84	44	4.06	1.1
28	60	2.21	0.6	60	28	2.93	0.6
36	84	1.97	0.9	84	36	2.73	1.0
44	100	1.93	1.1	100	44	2.24	1.1

the maximum tractive effort H_{m0} and the total motion resistance R_0 of the vehicle, which includes the resistance of the drivetrain and the soil through which the vehicle is moving [2]

$$DP = H_{m0} - R_0. \quad (2)$$

The DP of the DUKW-Ling can be estimated from the maximum incline tests. When a vehicle is operating on a slope, the maximum tractive force that the vehicle can develop is proportional to the maximum tractive force that can be developed on a level surface, in the same ratio as the load normal to the slope to the vehicle weight on a level surface [3], i.e.,

$$H_m(\theta) = H_{m0} \left(\frac{\Delta \cos \theta}{\Delta} \right) = H_{m0} \cos \theta \quad (3)$$

where Δ is the vehicle's weight (displacement) and θ is the angle of the slope. The tractive force required to climb a slope at constant speed with no slip is given by

$$H = \Delta \sin \theta + R_0 \cos \theta. \quad (4)$$

Thus, the maximum slope θ_{\max} trafficable by a tracked vehicle can be determined by equating the DP and maximum tractive force along a slope

$$\begin{aligned} H_{m0} \cos \theta_{\max} &= (DP + R_0) \cos \theta_{\max} \\ &= \Delta \sin \theta_{\max} + R_0 \cos \theta_{\max} \rightarrow \boxed{DP = \Delta \tan \theta_{\max}} \end{aligned} \quad (5)$$

Based on the tests conducted, the DP of the vehicle is 997 N.

d) Course keeping ability and motor control compensation: In testing, it was found that owing to a little additional friction on one side of the drivetrain, the vehicle tracked slightly to port when both motors are given the same command. To

compensate for this straight-line tracking error, a correction bias was added to the port motor open-loop control software. Through experimentation, this correction bias was found to be a constant difference of 4% of full speed. For example, giving a motor command of 60% to port and 56% to starboard resulted in straight tracking.

2) Land-Based Maneuvering Tests:

a) Circle tests: Traditional turning circle tests [1] were performed to determine tactical diameter. Speed loss, roll angle, and yaw rates were also recorded during these tests. During each test, the vehicle began with a straight-line forward motion until steady state was reached, then differential motor commands were applied to produce a turning circle. The vehicle's response (position, velocity, heading, and the rate of turn) was measured using the IMU, GPS, and compass. The motor controllers were also used to record motor commands, current, and voltage to the motors as each test was performed.

b) Turning radius: The first value that was defined in these tests is the resulting turning radius for a particular motor input. Table V gives the resulting turning radii and corresponding speeds during the circle maneuver for each differential motor command combination. The values are listed from largest to smallest. During some aggressive turning maneuvers, the tracks were observed to skip along their guide wheels and so tests with differential motor commands beyond the combination of 44% and 100% were avoided.

An example of a turning circle test can be seen in Fig. 11; the turning radius is taken as half of the mean of the measured north-south and east-west diameters.

For a starboard turn at motor commands of 100% port, 44% starboard, a minimum turning radius of 2.24 m was found. Similarly, for a port turn at motor commands of 44% port, 100% starboard, a turning radius of 1.93 m was found. Thus, the average minimum turning radius is 2.09 m.

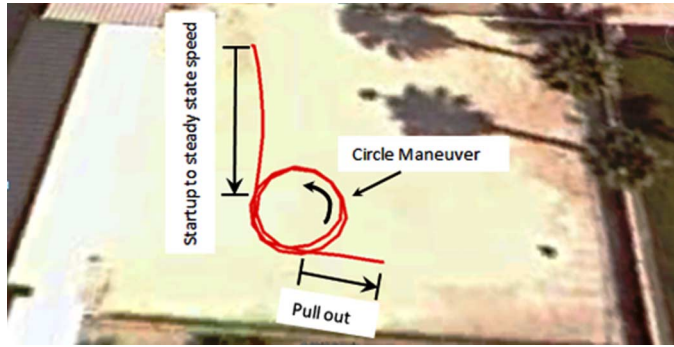


Fig. 11. Example turning circle maneuver on land.

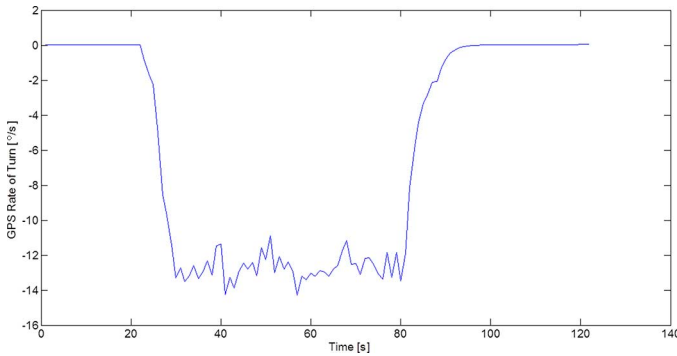


Fig. 12. Yaw rate from IMU in port turn.

TABLE VI
YAW RATE: LAND-MOTOR COMMAND VALUES ARE GIVEN
AS A PERCENTAGE OF FULL SCALE

Left Turn			Right Turn		
Port %	Stbd %	Yaw Rate [°/s]	Port %	Stbd %	Yaw Rate [°/s]
60	84	-4.84	84	60	2.77
28	44	-7.35	44	28	6.42
36	60	-9.66	60	36	7.35
44	84	-12.72	84	44	7.41
28	60	-14.11	60	28	8.66
36	84	-22.08	84	36	14.61
44	100	-24.58	100	44	17.67

c) *Yaw rate*: Fig. 12 is an example of the yaw rate measured during a turning circle test on land. A negative yaw rate indicates a port turn, or a counterclockwise rotation.

The slight variation of yaw rate during the circle test in Fig. 12 is mainly caused by the uneven sandy ground in the test area. It can be seen when the vehicle is at rest both before and after the turn that this fluctuation is not due to sensor noise, as the rate is constant when the vehicle is stationary. Table VI shows the average yaw rates found for each test.

d) *Land zigzag tests*: The zigzag test is a standard maneuvering experiment [1]. Zigzag test results are useful for the development of a dynamic model of the vehicle through system identification (see Section IV). The tests were performed on the beach on a flat area of sand using open-loop control, with five combinations of motor commands (Table VII). Each alternating differential thrust motor command combination was executed with a period of 10 s in a series of 30-s runs. An example of the measured yaw rate and motor commands is shown in Fig. 13. In

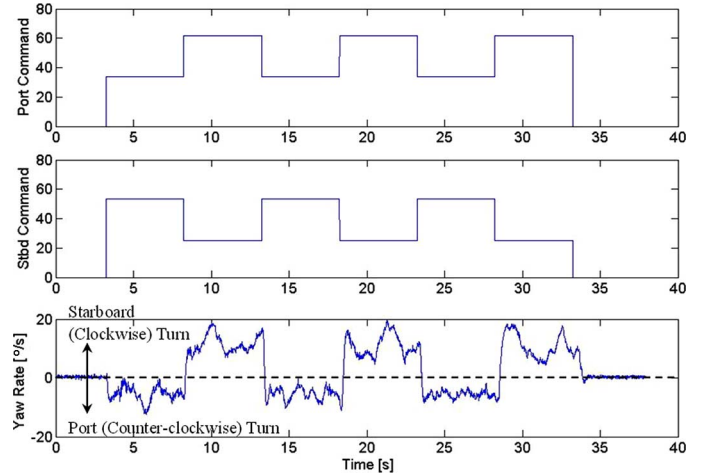


Fig. 13. Example zigzag test. The port and starboard commands are given as a percentage of the full-scale motor controller input value. The corresponding output yaw rate of the vehicle is shown in the lowermost plot.

TABLE VII
LAND ZIGZAG TEST MOTOR COMMANDS VALUES ARE GIVEN
AS A PERCENTAGE OF FULL SCALE

Test	High Value %	Low Value %
1	56	32
2	88	56
3	88	64
4	100	64
5	100	80

this figure, one can see an asymmetry in the yaw rate that was observed during the test, despite the motor command bias correction. The asymmetry may be the result of a slight difference in performance between the steady state and dynamic behavior of the system or a change in drivetrain friction from one test day to another, which may have occurred due to sand intrusion.

B. Water-Based Tests

As mentioned above, the vehicle was tested in a section of the Intracoastal Waterway in Dania Beach, FL, USA. This area is sheltered from wind and has minimal boat traffic to affect testing. The vehicle experienced only minor, wind-generated waves, as can be seen in Fig. 14. The wind speed and direction were also collected during all testing, and appear to have had no measurable effect on the vehicle test results.

1) *Steady-State Tests*: As in land testing, water tests also showed the vehicle was unable to track a perfectly straight course under open-loop control without a motor command bias correction. This may be caused by either: a) a mismatch in the output thrust generated by each trolling motor for a given input command; or b) propeller “walk”; since the propellers both spin in the same direction (counterclockwise), they create a force on the aft part of the vehicle to the port side, which can cause a slight starboard turn. Fig. 15 shows a track of the vehicle’s position. The wind was actually opposing starboard tracking, as it was coming out of the southwest at 2.59 m/s, and that is the direction into which the vehicle is tracking. Thus, it is clear that the slight turning motion is not related to wind effects. A



Fig. 14. The DUKW-Ling during waterborne testing. Note that the bulbous part of each hull is completely submerged and the waterline is located approximately halfway down the upper, wall-sided sections of each hull.

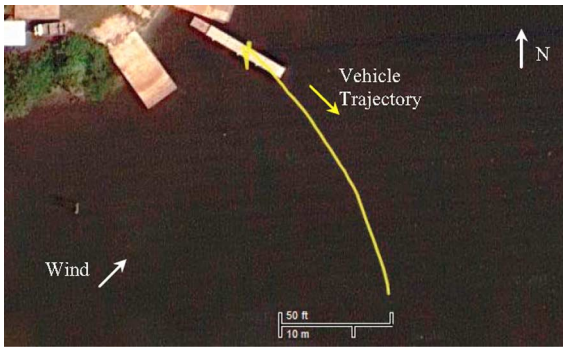


Fig. 15. Equal motor commands in water.

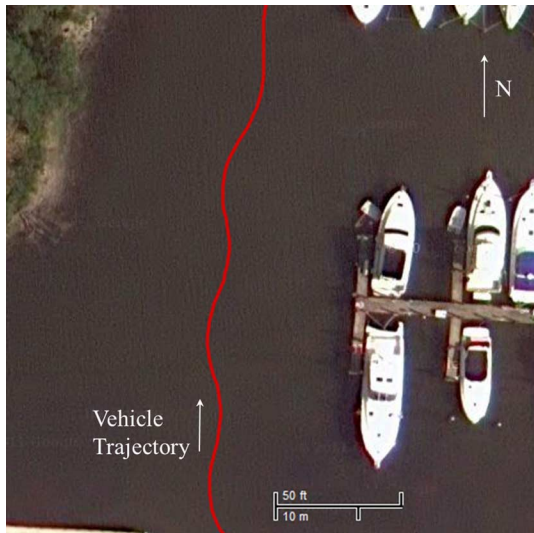


Fig. 16. Vehicle trajectory during the zigzag test.

bias correction factor of 4% was found to enable the vehicle to track straight under open-loop control.

2) Water-Based Maneuvering Tests:

a) *Circle tests:* As in the land-based testing described above, turning circle tests were initiated after the vehicle reached a steady-state straight-line motion. Table VIII shows the different combinations of motor commands provided to the propellers and the resulting turning radius and yaw rate for each test case. Note that, taken together, the yaw rate and turning

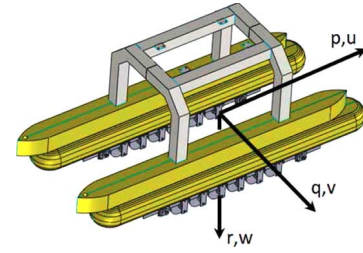


Fig. 17. Body-fixed maneuvering coordinate system.

radii can be used to estimate the speed of the vehicle during each circle maneuver.

The motor commands used were chosen to produce turns that would be expected in operation. Large radius turns were not performed because they were considered unnecessary; the largest radius tested was 11.75 m. As in the land tests, the GPS, IMU, and compass and motor controllers were used to collect data. Unlike the land tests, however, the wind speed and direction were also recorded to understand if windage affected the turning path of the vehicle.

Each turning radius was found by averaging the north–south and east–west radii encountered during a turning circle maneuver. The tightest turns are executed when one motor is in forward and the other is in reverse. As the vehicle’s drivetrain is not retractable, it sticks out under the hulls and acts like a keel, which helps with straight-line tracking, but negatively affects the vehicle’s tight turning radius. Looking at the lower turning radii shown in the tables above, one can see that the larger the command to the reverse motor, the smaller the turning radius.

b) *Water zigzag tests:* As described in the land zigzag tests, the water zigzag tests were performed using a combination of differential thrust commands and were performed to obtain data that would be useful for system identification. The GPS, IMU, and compass and motor controllers were used to collect data during the tests. Fig. 16 is a plot of the vehicle’s position during the water zigzag test for motor commands of 100% and 0%.

IV. SYSTEM IDENTIFICATION

Data collected from the landborne and waterborne zigzag tests in Sections III-A2b and III-B2b, respectively, were used to develop three degree-of-freedom, state–space maneuvering models for the vehicle in a state–space form

$$\begin{aligned}\vec{x}(t_{n+1}) &= A\vec{x}(t_n) + B\vec{u}(t_n) \\ \vec{y}(t_n) &= C\vec{x}(t_n) + D\vec{u}(t_n).\end{aligned}\quad (6)$$

Here, \vec{x} is a state vector; A , B , C , and D are matrices of constant coefficients; \vec{u} is an input vector of motor commands given as a percentage of the full-scale value

$$\vec{u} = \begin{pmatrix} \text{port_cmd} \\ \text{stbd_cmd} \end{pmatrix}; \quad (7)$$

and \vec{y} is the output vector of surge speed u , sway velocity v , and yaw rate r in body-fixed maneuvering coordinates (Fig. 17)

$$\vec{y} = \begin{pmatrix} u \\ v \\ r \end{pmatrix}. \quad (8)$$

TABLE VIII
TURNING RADII AND YAW RATE IN WATER. A NEGATIVE YAW RATE INDICATES A PORT TURN (COUNTERCLOCKWISE ROTATION)

Left Turn				Right Turn			
Port %	Stbd %	Radius [m]	Yaw Rate [°/s]	Port %	Stbd %	Radius [m]	Yaw Rate [°/s]
0	80	11.75	-2.66	80	0	9.15	4.75
0	100	11.05	-3.20	100	0	8.96	4.91
0	64	10.85	-3.62	64	0	7.84	5.62
-32	80	8.62	-3.80	80	-32	7.54	5.73
-36	100	7.81	-4.90	100	-36	6.88	5.82
-64	80	5.28	-5.66	80	-64	6.62	6.08
-80	80	3.13	-7.29	80	-80	4.70	7.01
-100	100	2.52	-9.29	100	-100	4.52	8.05

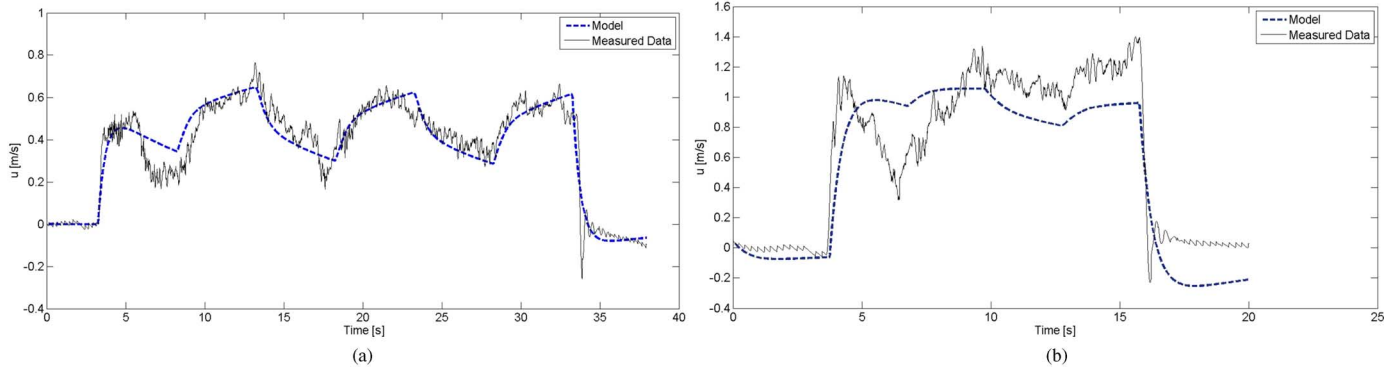


Fig. 18. (a) Body fixed u velocity model and original data. (b) Validation case.

TABLE IX
WATER ZIGZAG TEST MOTOR COMMANDS VALUES ARE GIVEN AS A PERCENTAGE OF FULL SCALE

Test	High Value %	Low Value %
1	80	0
2	100	0
3	100	16
4	100	40

Note that the state vector identified by the system ID approach conducted here is generated by a “black box” nonparametric identification method. The terms in the state vector can be obtained by solving (6) for $\vec{x}(t)$. However, as the state vector is determined nonparametrically, the terms in $\vec{x}(t)$ do not necessarily correspond to any specific physical inputs or outputs.

As the vehicle’s instrumentation records data in an Earth-fixed, north-west-up coordinate system, the measured velocities were transformed to a body-fixed reference frame centered at the center of gravity of the vehicle. A commercial software package (the System Identification Toolbox from Mathworks, Inc., Natick, MA, USA) was used to identify the parameters in the coefficient matrices A , B , C , and D in (6), which provided the best match between the measured and simulated outputs \vec{y} for the same measured inputs. While each model was developed primarily using one set of input-output data, other sets of input-output data from different zigzag maneuvering tests were used for validation (see Tables VII and IX). The state-space model developed for the landborne system was determined using measurements from tests with alternating

track motor input commands of 56% and 32%. The state-space model developed for the waterborne system was determined using measurements from tests with alternating propeller motor input commands of 80% and 0%. The sample period for both the landborne and waterborne state-space models is 0.01 s.

A. Land

A third-order linear state-space model with coefficient matrices of the form

$$\begin{aligned}
 A &= \begin{bmatrix} 0.9979 & -4.338 \times 10^{-3} & -0.5499 \times 10^{-3} \\ -5.26 \times 10^{-3} & 0.9796 & 2.046 \times 10^{-3} \\ 13.16 \times 10^{-3} & 10.08 \times 10^{-3} & 0.9541 \end{bmatrix} \\
 B &= \begin{bmatrix} -1.671 & 15.09 \\ 3.967 & 58.54 \\ 101.4 & -59.95 \end{bmatrix} \times 10^{-6} \\
 C &= \begin{bmatrix} 3.78 & 3.127 & 1.011 \\ 7.331 & -1.915 & -0.8544 \\ -0.5503 & -1.281 & 2.588 \end{bmatrix} \\
 D &= \begin{bmatrix} 0 & 0 \\ 0 & 0 \\ 0 & 0 \end{bmatrix}
 \end{aligned}$$

was found to provide the best fit to the measured data. The u , v , and yaw rate outputs of the 56% and 32% land-based zigzag test, with an overlay of the final model that was obtained on the outputs are shown in Figs. 18–20; also shown is the corresponding validation case using experimental data from the 100% and 80% land-based zigzag tests.

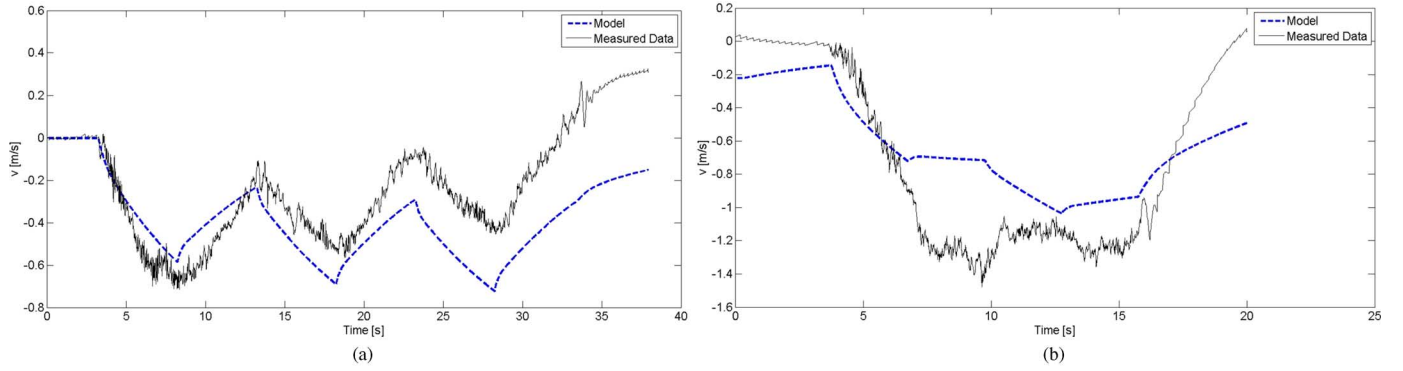


Fig. 19. (a) Body fixed v velocity model and original data. (b) Validation case.

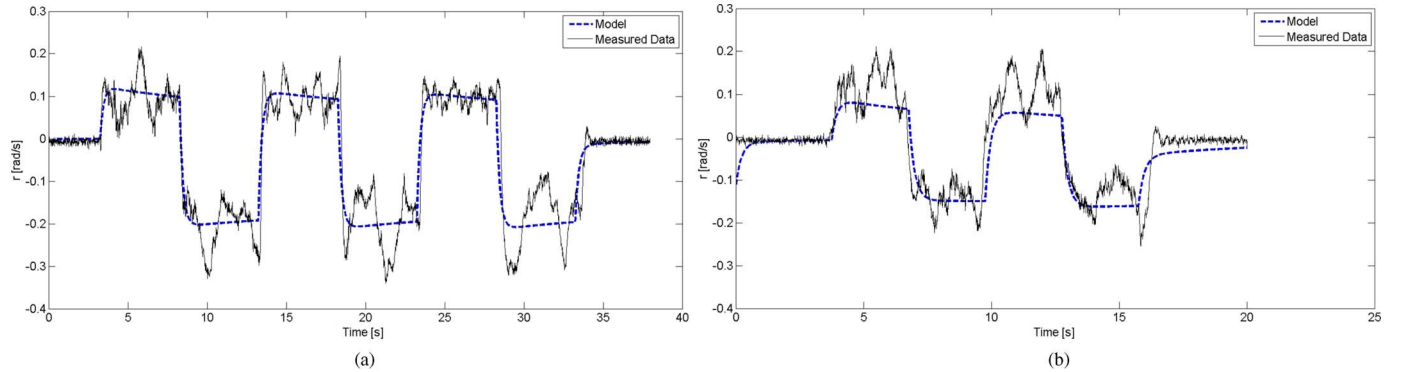


Fig. 20. (a) Yaw rate model and original data. (b) Validation case.

B. Water

A third-order linear state-space model with the coefficient matrices of the form

$$\begin{aligned}
 A &= \begin{bmatrix} 0.9984 & 0.2284 \times 10^{-3} & 0.2442 \times 10^{-3} \\ -1.167 \times 10^{-3} & 0.9999 & 9.626 \times 10^{-5} \\ 0.8616 \times 10^{-3} & -1.249 \times 10^{-3} & 0.9965 \end{bmatrix} \\
 B &= \begin{bmatrix} 0.5909 & 0.4656 \\ 0.2151 & 0.5388 \\ -1.333 & 0.5398 \end{bmatrix} \times 10^{-6} \\
 C &= \begin{bmatrix} 28.68 & -1.485 & -0.038 \\ -3.195 & 11.03 & 0.020 \\ -0.018 & -1.431 & -2.948 \end{bmatrix} \\
 D &= \begin{bmatrix} 0 & 0 \\ 0 & 0 \\ 0 & 0 \end{bmatrix}
 \end{aligned}$$

was found to provide the best fit to the measured data. The u , v , and yaw rate outputs of the 80% and 0% water-based zigzag test, with an overlay of the final model that was obtained on the outputs are shown in Figs. 21–23; also shown is the corresponding validation case using experimental data from the 100% and 0% water-based zigzag tests.

V. SEAKEEPING

A. Natural Frequencies of Roll, Pitch, and Heave

For later comparison with the dominant frequencies of the waves that the vehicle will encounter in the surfzone transition

region, the natural frequencies of the vehicle's roll, pitch, and heave responses are measured at zero forward speed in calm water. For example, in roll response tests, the vehicle is given a small amplitude motion in the roll direction by pushing down on the middle of one hull and releasing it. The IMU is used to collect the resulting motion data, which are then used to find the damped natural frequency of the motion. Each test was performed five times and the results have been averaged.

The roll response [Fig. 24(a) and (b)] is found to be uncoupled from the pitching and heaving responses and has the form of an exponentially decaying sinusoid. The damped and undamped roll frequencies are related by (9), where ω_D is the damped frequency, ω_N is the undamped natural frequency, and ζ is the damping ratio

$$\omega_D = \omega_N \sqrt{1 - \zeta^2}. \quad (9)$$

The response data are used to determine the damping ratio ζ and logarithmic decrement δ with the following relationships:

$$\zeta = \frac{1}{\sqrt{1 + \left(\frac{2\pi}{\delta}\right)^2}} \quad (10)$$

$$\delta = \frac{1}{n} \ln \left(\frac{x_0}{x_n} \right). \quad (11)$$

δ is found by comparing the amplitudes of two peaks measured in the data. x_0 is the larger of the two amplitudes, and x_n is the smaller amplitude. The value n is the number of periods separating the two amplitudes. In Fig. 24, x_0 , x_n , and n are shown. The average damped frequency of the roll response is found to

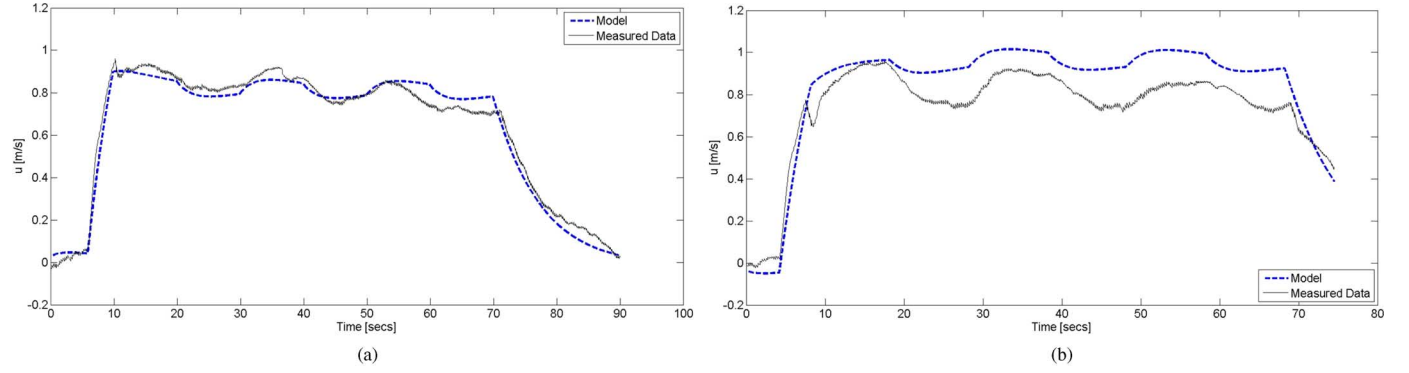
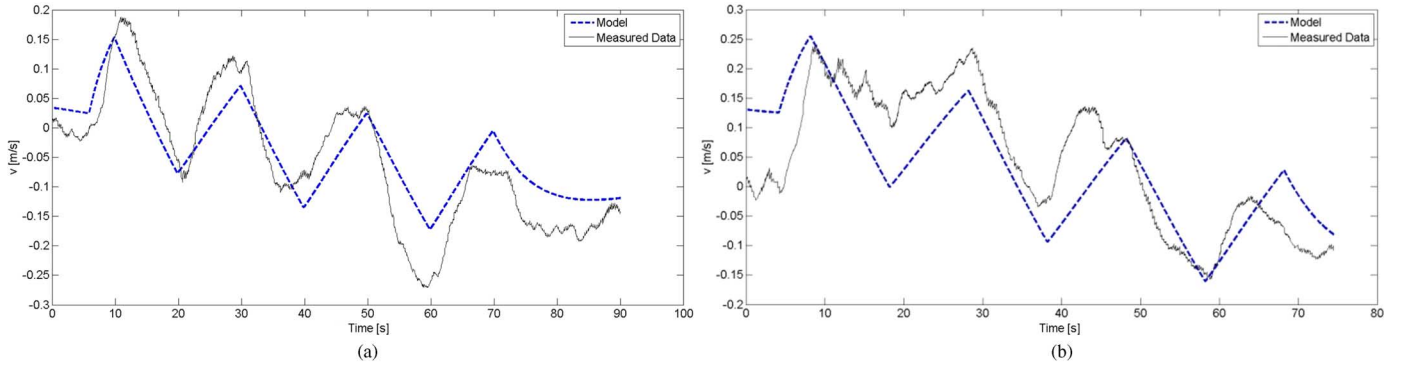
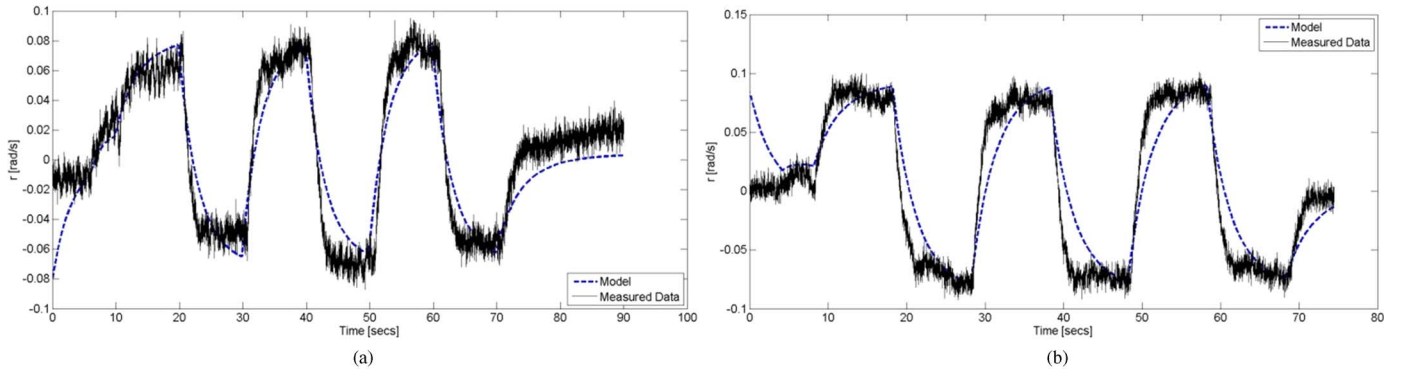
Fig. 21. (a) Body fixed u velocity model and original data. (b) Validation case.Fig. 22. (a) Body fixed v velocity model and original data. (b) Validation case.

Fig. 23. (a) Yaw rate model and original data. (b) Validation case.

be 0.3906 Hz, which corresponds to an undamped natural frequency of $f_{n_roll} = 0.3925$ Hz.

Plots of the phase difference between the pitch and heave responses [Fig. 25(a)] to a pitch input show that there is a period of time (close to ten heave response cycles) over which the phase difference ψ is approximately constant [Fig. 25(b)], indicating that the two motions are coupled.

The pitch–heave coupling is likely the result of the vehicle’s fore–aft asymmetry. Examination of the power spectrum of the coupled response (Fig. 26) reveals that the dominant responses occur at damped frequencies of 0.5731 and 0.6336 Hz; the vessel’s pitch and heave motion will be excited at these frequencies. As shown in [4], the undamped natural frequency in heave of a monohull can be estimated as

$$f_{n_heave} = \frac{1}{2\pi} \sqrt{\frac{\rho g A_W}{M + A_{33}}} \quad (12)$$

where ρ is the density of seawater, g is gravity, M is the mass of the vessel, and A_{33} is the added mass in heave. If the diameter of the underwater SWATH hull and the LOA of the vehicle are used to estimate A_{33} via the strip theory for a deeply submerged circular cylinder, the theory gives $f_{n_heave} = 0.5439$ Hz. As this value is close to 0.5731 Hz and the natural pitch frequency of a vessel tends to be higher than that of the natural heaving frequency, the natural frequency of heave will be taken as $f_{n_heave} = 0.5731$ Hz and the natural frequency of pitch will be taken as $f_{n_pitch} = 0.6336$ Hz.

B. Wave Characteristics

Images of the surfzone at the test site on each day of testing are shown in Fig. 27(a) and (b). On the first test day the waves had a significant waveheight of $H_{1/3} = 28$ cm (calculated as four times the standard deviation of the measured waveheight [4]). Sea conditions were calmer on the second test day with a

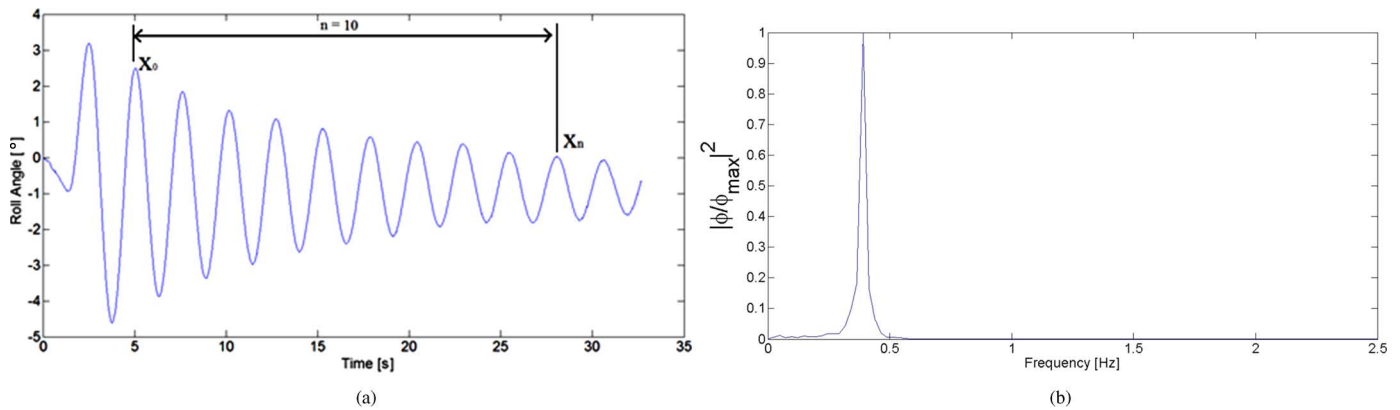


Fig. 24. Roll response to roll input (a) time series and (b) normalized power spectrum.

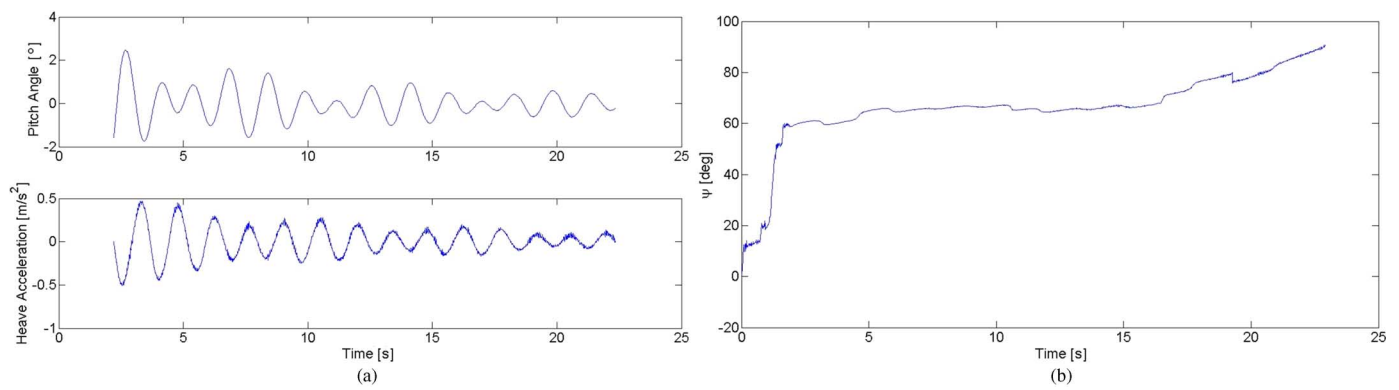


Fig. 25. (a) Time series pitch and heave response to pitch input and (b) measured phase angle between pitch and heave responses.

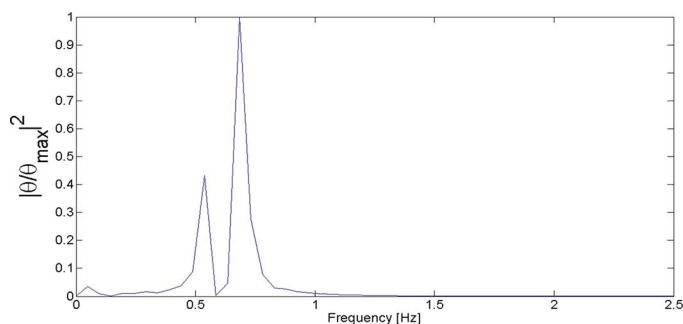


Fig. 26. Normalized power spectrum of the pitch response to a pitch input.

significant waveheight of $H_{1/3} = 8$ cm. On both test days, the propagation direction of the incoming waves was approximately perpendicular to the beach.

Two capacitive wave gauges were mounted in the surfzone to characterize the heights and frequencies of the incoming waves. These sensors are typically used to measure the vertical displacement of a free surface with respect to the still waterline. However, because these tests were performed in an uncontrolled environment, determination of the still waterline was not possible. Instead, the average value of the free surface over each 3-min run was used as a zero location, and the wave amplitudes were measured with respect to this position. The wave gauges were placed near the trajectory of the DUKW-Ling during the

surfzone tests, at distances of about 6 and 9 m from the waterline, in water depths of about 0.76 and 0.91 m. The data were collected at a sample rate of 20 Hz.

To examine the frequency content of the waves in the surfzone tests, the power spectra of the wave field time series measurements were calculated. Data typical of the wave field time series and power spectra are shown in Figs. 28 and 29, respectively.

The power spectrum in Fig. 29 is representative of the wave field data collected on the first day of testing. The dominant wave frequency was found to be near 0.29 Hz and about 50% of the energy in the power spectrum was found to occur within a frequency range of $0.18 \leq f \leq 0.40$ Hz (wave periods of $2.50 \leq T \leq 5.69$ s). At a depth of 0.76 m, the wavelength corresponding to the dominant frequency of 0.29 Hz would be 9.08 m.

The power spectrum in Fig. 30 is representative of the wave field data collected on the second day of testing. The dominant wave frequency was found to be near 0.27 Hz and about 50% of the energy in the power spectrum was found to occur within a frequency range of $0.13 \leq f \leq 0.42$ Hz (wave periods of $2.40 \leq T \leq 7.59$ s). The waves appear to be more monochromatic than on test day 1. At a depth of 0.76 m, the wavelength corresponding to the dominant frequency of 0.27 Hz would be 9.60 m.

The natural frequencies of roll, pitch, and heave identified in Section V-A have been labeled in both Figs. 29 and 30. f_{n_roll} lies within the range of dominant frequencies observed in the

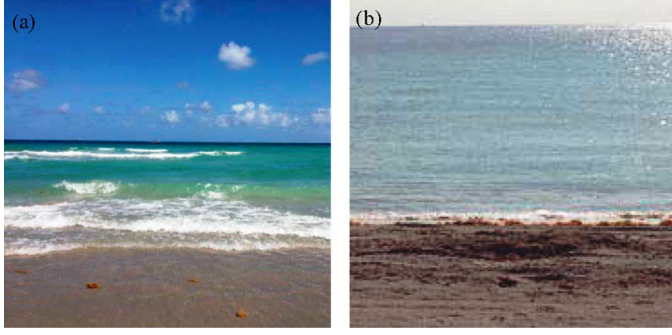


Fig. 27. Dania Beach on (a) test day 1 ($H_{1/3} = 28$ cm) and (b) test day 2 ($H_{1/3} = 8$ cm).

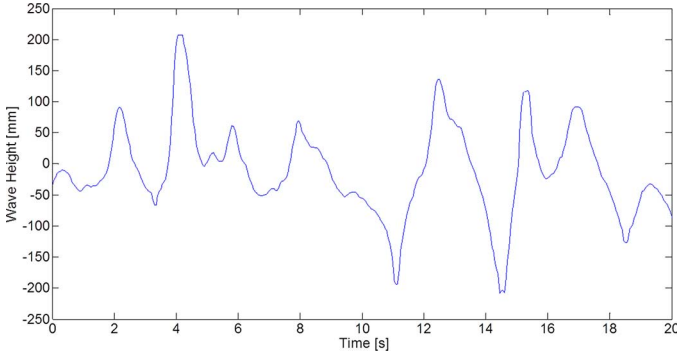


Fig. 28. A 20-s segment of representative wave measurement data recorded on test day 1, when $H_{1/3} = 28$ cm.

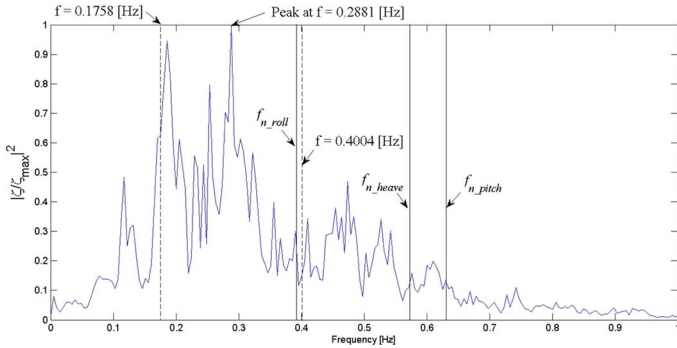


Fig. 29. Representative example of the power spectral density of waves in the surfzone for $H_{1/3} = 28$ cm. As indicated by the vertical dashed lines, 50% of the measured wave energy occurs in the frequency band between $0.18 \leq f \leq 0.40$ Hz (wave periods of $2.50 \leq T \leq 5.69$ s).

surfzone. Thus, one can expect to see the resonant mode of the vehicle's roll response excited by the waves present. Additionally, as f_{n_heave} and f_{n_pitch} are higher than the range of dominant frequencies observed in the surfzone, heave and pitch resonances are unlikely to be excited, but there will be minimal attenuation of wave-induced heave and pitch response.

1) *Wave Scaling*: The waveheights can be scaled geometrically based on the 1/7th-scale size of the vehicle model. However, the wave period should be scaled as shown in (13), where T_{Full} and T_{model} are the wave periods of the full-scale vehicle and model, respectively [13]. On the day of the 28-cm significant waveheight tests, the measured waves would correspond to full-scale waves, which have 1/3 significant heights of approximately 2 m and periods of $6.61 \leq T_{Full} \leq 15.1$ s; these values

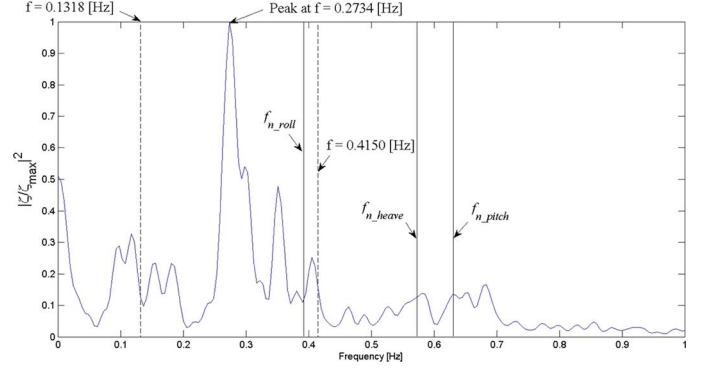


Fig. 30. Representative example of the power spectral density of waves in the surfzone for $H_{1/3} = 8$ cm. As indicated by the vertical dashed lines, 50% of the measured wave energy occurs in the frequency band between $0.13 \leq f \leq 0.42$ Hz (wave periods of $2.40 \leq T \leq 7.59$ s). The peak which occurs near the origin indicates that the waves are superposed upon a slow swell with a period of about 290 s.

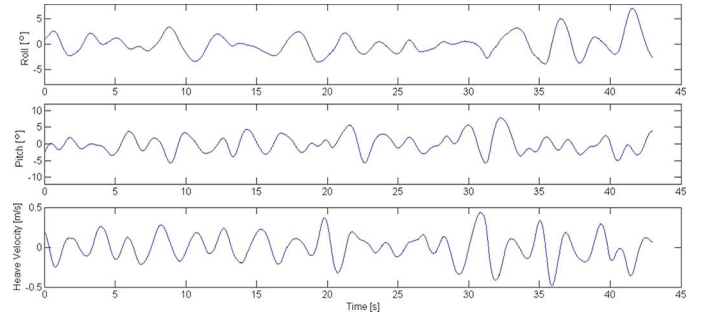


Fig. 31. Representative vehicle motions in the surfzone on test day 1.

correspond to approximately sea state 2 conditions in the North Atlantic [4]

$$T_{Full} = \frac{T_{model}}{\sqrt{\text{Scale Factor}}} \quad (13)$$

C. Vehicle in the Surfzone

To explore the response of the vehicle to breaking waves and surge forces, the DUKW-Ling was allowed to drift in a surfzone while completely waterborne. IMU and DGPS data were collected to measure the acceleration, rotation rates, and velocity experienced by the vehicle. With the available equipment, it was not possible to also measure the wave characteristics near the vehicle during the tests. A representative time series of the vehicle motion in the surfzone is shown in Fig. 31. The test was performed five separate times during each test day, but for simplification of reporting, only one data set is shown. The vehicle was loosely restrained such that it pointed toward the beach and experienced following waves; the yaw angle oscillated about its mean value by approximately $\pm 8^\circ$.

The corresponding power spectrum of the vehicle's frequency response is shown in Fig. 32. The heave, roll, and pitch responses do not show significant motion at f_{n_heave} and f_{n_pitch} . However, the roll response appears to exhibit motion at f_{n_roll} . The pitch and heave responses possess peaks in their power spectra at frequencies of 0.26 and 0.45 Hz; the roll response has two large peaks at 0.24 and 0.33 Hz. These peaks

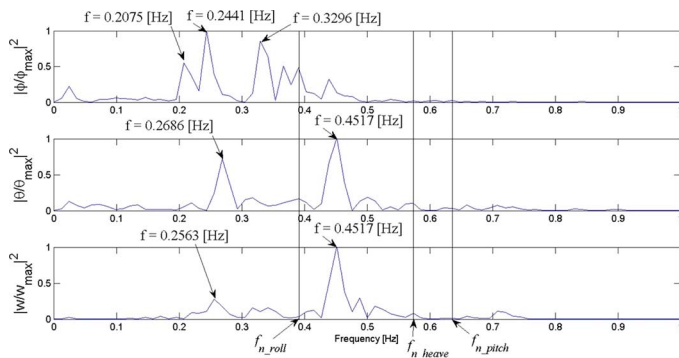


Fig. 32. Power spectral density plots of the roll $|\phi/\phi_{\max}|^2$, pitch $|\theta/\theta_{\max}|^2$, and heave velocity $|w/w_{\max}|^2$ responses in the surfzone on test day 1. The natural frequencies of pitch, heave, and roll are labeled with solid vertical lines.

TABLE X
Vehicle Motions in the Surfzone Test Day 1—Average of All Tests

Value	RMS	Standard Deviation
Heave Velocity [m/s]	0.18	0.02
Pitch Angle [°]	2.79	0.40
Roll Angle [°]	2.19	0.49
Yaw Rate [°/s]	5.99	0.24

TABLE XI
Vehicle Motions in the Surfzone Test Day 2—Average of All Tests

Value	RMS	Standard Deviation
Heave Velocity [m/s]	0.11	0.04
Pitch Angle [°]	1.60	0.39
Roll Angle [°]	1.35	0.09
Yaw Rate [°/s]	5.15	1.08

may correspond to excitation frequencies in the surfzone waves that were not also present closer to shore where the wave field measurements reported above (see Section V-B) were recorded.

The surfzone vehicle response data are summarized in Tables X and XI, which give the average root mean square and its standard deviation for the measured heave velocity, pitch angle, roll angle, and yaw rate across all five tests on each test day.

VI. TRANSITION REGION EXPERIMENTS

The transition zone tests were performed on the beach in Dania Beach, FL, USA. In order for the vehicle to operate effectively, it cannot be used in waves which are too large. The maximum waveheight and surf conditions for operations were determined by trial and error. Based on experience, testing was restricted to significant waveheights of up to $H_{1/3} = 30$ cm.

The empirical relation (1) was used to determine the force on each track using the measured input current recorded at each drive motor during the beach transition experiments. The vehicle was driven under open-loop control across the surfzone with its tracks engaged from land to sea, as well as from sea to land. In these tests, the vehicle was propelled solely by the tracks; the propellers were turned off. Vehicle heading, acceleration, position, speed over ground, and motor command data were recorded, as were the wind speed/direction

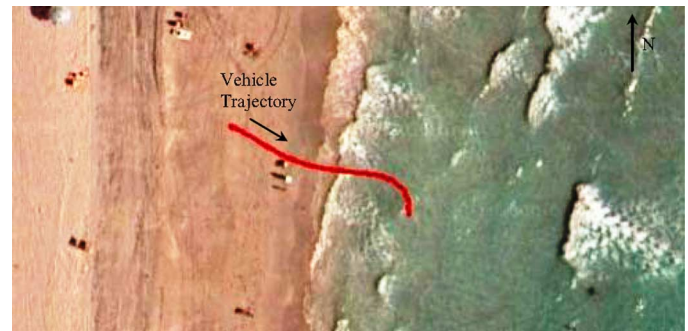


Fig. 33. Example land-to-sea vehicle track. Note that the satellite image of the test site was not taken at the same time as the testing was performed; the curved portion of the trajectory occurs after the land-to-sea transition test is complete and the buoyant vehicle has started to drift.

and wave characteristics. The DUKW-Ling was tested over a range of track speeds corresponding motor commands of 64%, 72%, 80%, 88%, and 100% of full scale (100% of full scale corresponds to a track speed of 2 m/s). The experiments were performed on both test day 1 and test day 2 (Section V-B), so that the vehicle could be tested in different wave conditions.

A. Land to Sea

As shown from the recorded GPS coordinates of the vehicle in Fig. 33, the land-to-sea transition tests were initiated with the DUKW-Ling facing the ocean and perpendicular to the mean waterline; note that at the time of testing the waterline at the beach was not the same as shown in the satellite photo. At the start of each test run, the vehicle was positioned about 2 m from the mean waterline.

Accounting for the motor command bias (see Section III-A1d), equivalent inputs were given to both the starboard and port tracks for 30 s during each run. The measured force required to drive each track for a motor command of 64% is shown in Fig. 34. The resulting roll, pitch, yaw rate, and heave velocity of the vehicle are presented in Fig. 35.

Looking at the data in Fig. 34, it can be seen that when the vehicle starts to move, the track force briefly peaks to almost double the force required to move the vehicle across the sand before it enters the water. This is due to the initial static friction in the drivetrain and between the track and sand that must be overcome. Similar peaks can be seen in the track force measurements of bulldozers [2] and are likely responsible for the characteristic lurch seen when tracked vehicles start to move from rest.

The track force stays fairly constant throughout the landborne stage, which is slightly less than 20 s into the test, when it begins to fall. By comparing the IMU motion data (Fig. 35) and the track forces (Fig. 34), it can be seen that track force begins to decrease as waves start to affect the vehicle. During this period, the DUKW-Ling is making the transition from trackborne to waterborne and ultimately becomes completely supported by the buoyancy of the hulls. The intermittent jumps in track force occurring during the first few seconds that the vehicle is waterborne may be attributed to the tracks coming into contact with the sand as waves cause it to heave.

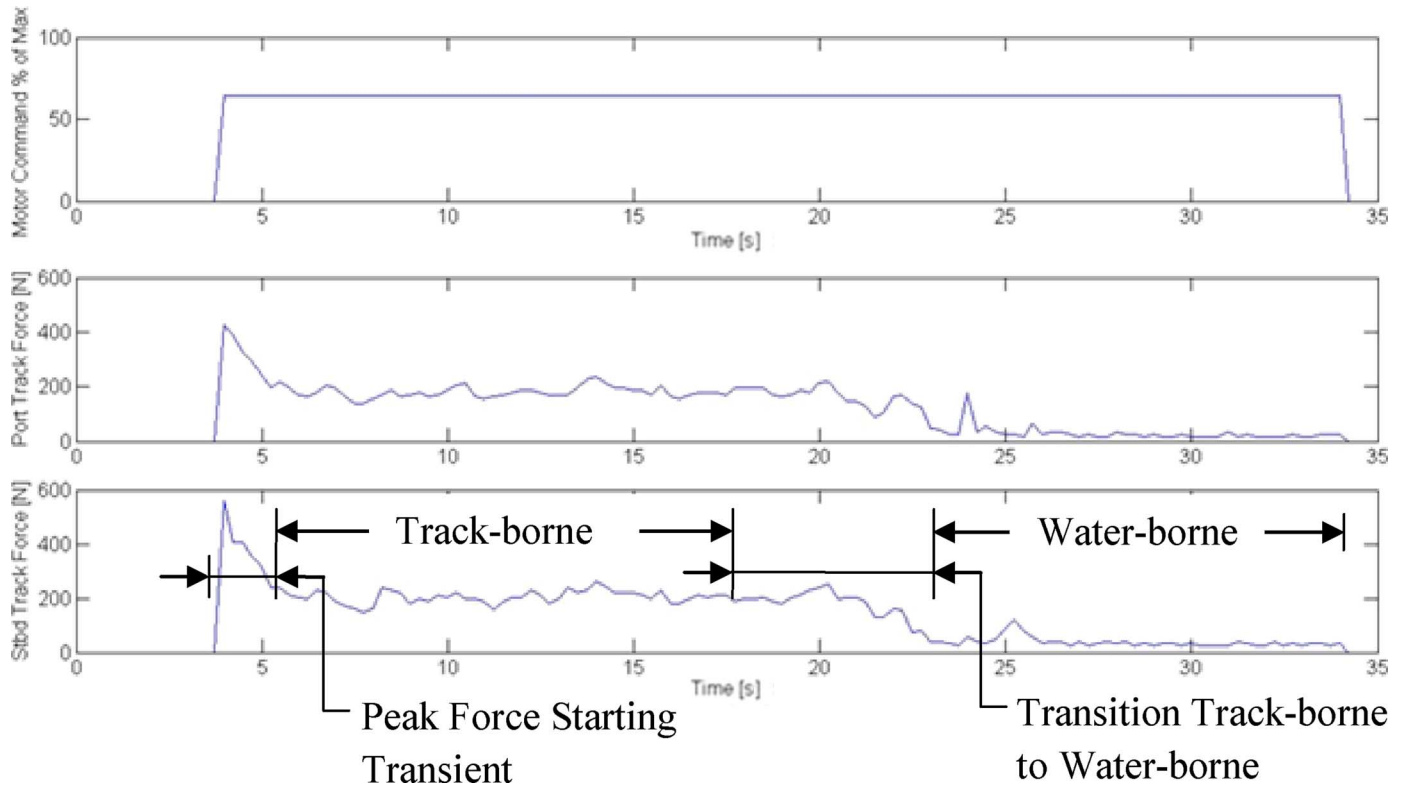


Fig. 34. Land-to-sea transition motor command input (64% of maximum value) and measured track force output for waveheights of $H_{1/3} = 28$ cm.

During the waterborne stage, the remaining track forces are caused by drivetrain friction. For all motor commands tested, the form of both the starboard and port track force curves was the same as is shown in Fig. 34. However, the force on each track during the trackborne segment of the transition increased as the commanded speed of the vehicle increased.

B. Sea to Land

Each test was initiated about 15 m from the mean waterline on the beach. At the start of each run, the floating vehicle was manually positioned so that it faced the beach with its treads approximately 30 cm above the sand. Once in position, the tracks were turned on and the vehicle was gently released so that the action of incoming waves pushed it toward the shore and into contact with the sand. The vehicle's trajectory is similar, but opposite in direction, to that shown in Fig. 33. The data collected during the sea-to-land transition are shown in Figs. 36 and 37. For comparison, the sea-to-land data are presented for a motor command of 64%, which was the same motor command used to collect the land-to-sea data shown in Figs. 34 and 35.

As might be expected, the form of the track forces and vehicle motion measurements mirror those of the land-to-sea transition. However, the magnitude of the transition zone track forces when the vehicle is moving from land to sea are lower than when the vehicle is moving from sea to land because the vehicle is essentially moving downhill when transitioning from land to sea and uphill when transitioning from sea to land. On test day 1 ($H_{1/3} = 28$ cm), the average land-to-sea force on each track in the trackborne segment of the transition zone ranged from about 180 to 280 N and the average sea-to-land

transition forces measured ranged from 260 to 403 N. On test day 2 ($H_{1/3} = 8$ cm), the average land-to-sea force on each track in the trackborne segment of the transition zone ranged from about 110 to 260 N, and the average sea-to-land transition forces measured ranged from 355 to 545 N. Note that the land-to-sea track forces are lower on test day 2 than on test day 1, while at the same time the sea-to-land track forces are higher on test day 2 than on test day 1. As revealed by an examination of the pitch data for each test day, a reason for this is that the slope of the beach at the test site was slightly steeper (approximately 3°) on test day 2. Additionally, it is possible that the larger waves present on test day 1 helped to push the vehicle onto shore, making the track forces in the transition zone lower in the sea-to-land transition zone.

VII. TRANSITION ZONE MODELING

A. Froude-Krylov Wave Excitation Forces

An examination of the surfzone wave field measurements suggests that the ratios of significant waveheight to wavelength of the most dominant waves are much smaller than the 1/7 ratio typically accepted as the upper limit for which deep-water waves start to become nonlinear and break. Here, the wave excitation forces acting on the vehicle in shallow water (0.76-m depth) are estimated using the Froude-Krylov strip theory approach. It is assumed that the vehicle is moving in head seas (encounter angle of 0°) at a forward speed of 1.1 m/s and that the incoming waves have a height of 28 cm and a period of 4.88 s, as do those reported in Section V-B. At this depth, the wave period corresponds to waves with a wavelength of 13 m. The

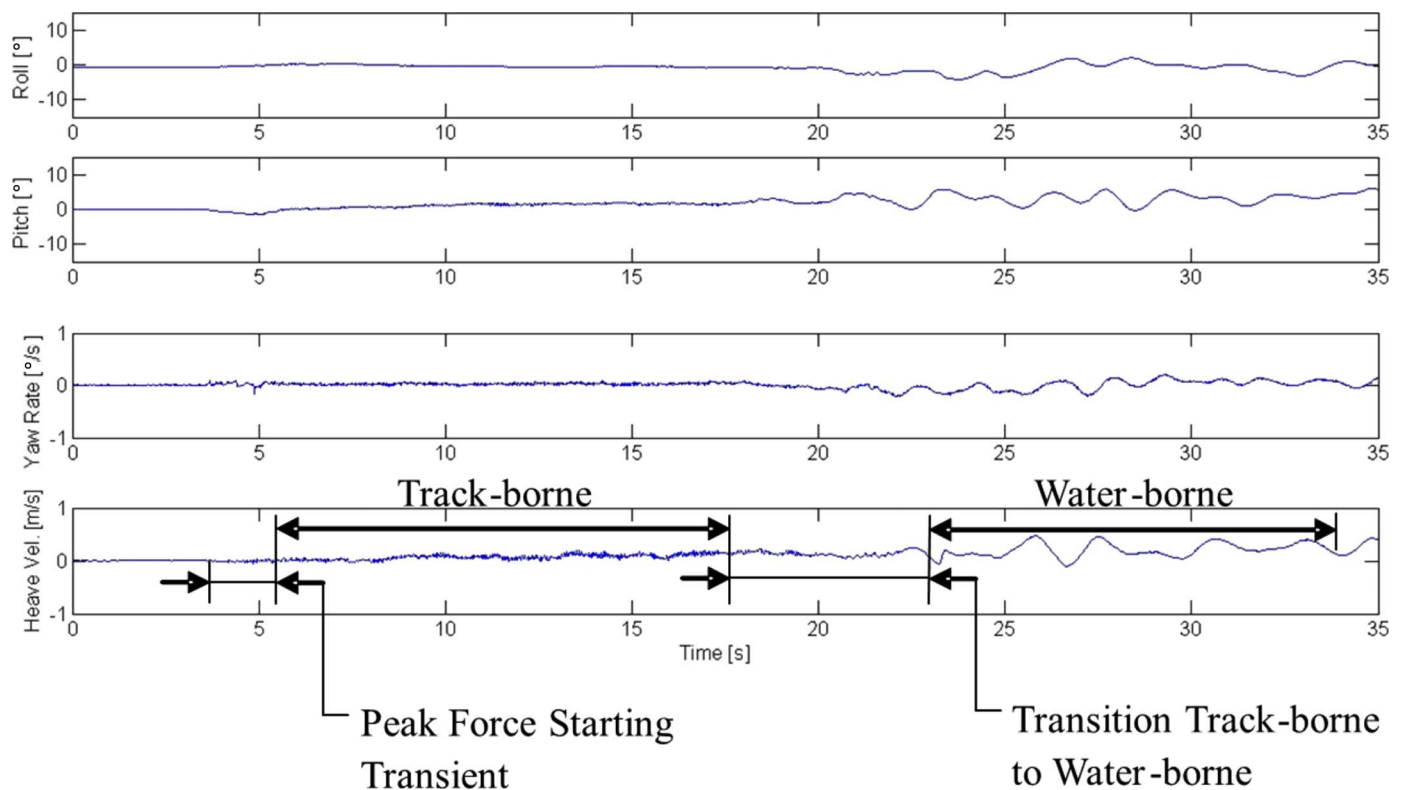


Fig. 35. Land-to-sea transition motions (motor command is 64% of full scale); waveheights of $H_{1/3} = 28$ cm.

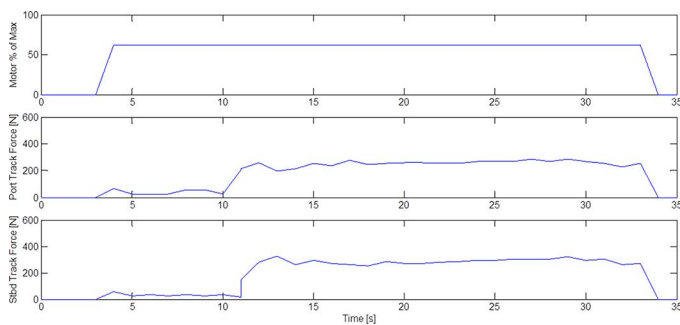


Fig. 36. Sea-to-land transition motor data (motor command: 64% of max).

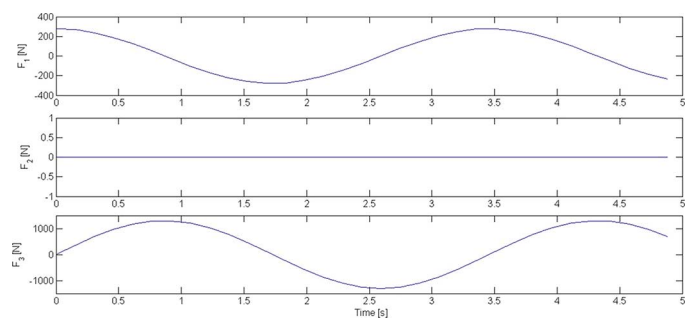


Fig. 38. Surge F_1 , sway F_2 , and heave F_3 forces versus time.

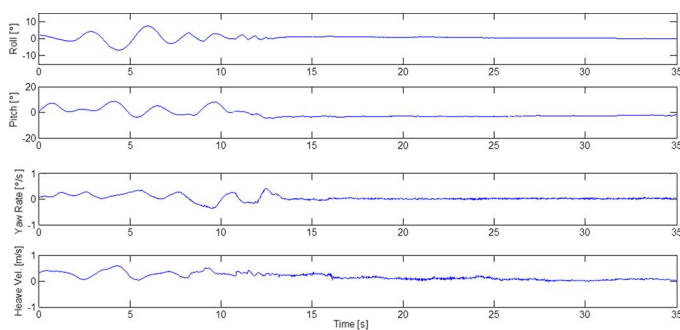


Fig. 37. Sea-to-land transition motions (motor command: 64% of max).

twin hulls are modeled as circular cylinders. End effects and hydrodynamic hull interaction effects are ignored. A standard seakeeping coordinate system for these calculations is located

amidships at the still waterline with the x_1 -axis pointing forward and the x_3 -axis pointing vertically upward. As shown in Figs. 38 and 39, the theory predicts that the amplitude of the surge forces acting on the vehicle is about 280 N and the amplitude of the pitching moment is approximately 390 N-m for these wave conditions.

The predicted magnitude of the wave-induced surge forces is slightly larger than the measured force on each vehicle track (see Section VI-A) when the DUKW-Ling is crossing the transition zone between the beach and the surfzone. Hence, as can be seen in Fig. 40 for those times between 15 and 20 s (just before the vehicle becomes hull supported), wave impacts will affect the forward speed of the vehicle and cannot generally be ignored when modeling its motion in waves.

To get an estimate for the velocity fluctuations induced by wave forces, we can assume that the vehicle is operating at constant velocity near the thrust-equals-drag condition, and that the

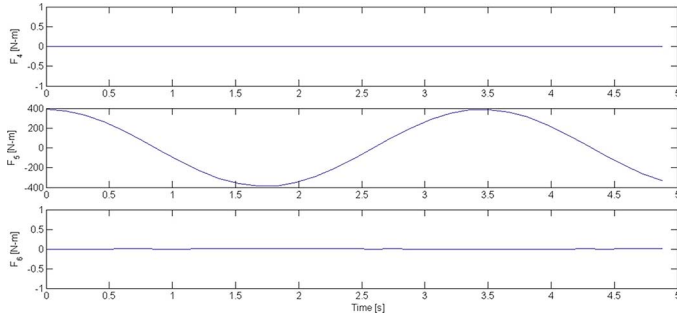
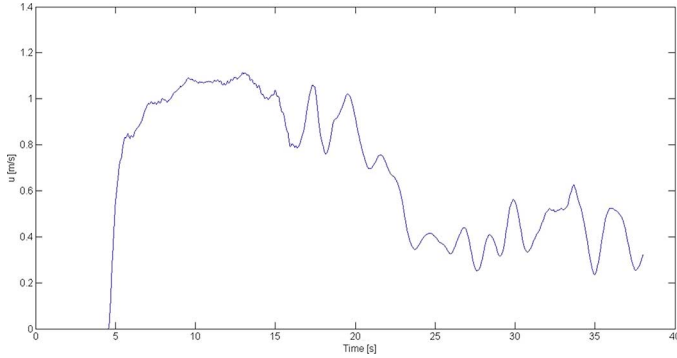
Fig. 39. Roll F_4 , pitch F_5 , and yaw F_6 moments versus time.

Fig. 40. Measured surge speed over ground during land-to-sea transition on beach in 28-cm waves.

departure from equilibrium is caused by wave forces. In this way, the velocity fluctuations can be estimated by integrating the wave-induced accelerations

$$\delta \ddot{x}_1 = \frac{F_1}{M} \rightarrow \delta \dot{x} = \delta u = \int \frac{F_1}{M} dt \quad (14)$$

where M is the mass of the vehicle, x_1 is the coordinate in the surge direction, and u is the surge speed. As shown in Fig. 41, the magnitude of the predicted surge velocity fluctuations is about 0.5 m/s. If we assume that a closed-loop speed controller is able to compensate for the speed variation to maintain a constant forward velocity, and imposes a track force on each tread of up to 35 N to counter the velocity fluctuations, the fluctuations can be slightly reduced to a magnitude of about 0.3 m/s (Fig. 41). The magnitude of this velocity fluctuation estimate is of the same order as that measured in Fig. 40, and given that added mass and damping effects are ignored, suggests that the approach might provide a good first estimate for design purposes.

B. Transition Zone Track Force Model

In the absence of specific information about the behavior of tracked vehicles in a beach transition zone, Flom [6] assumes that the tractive forces generated by the DUKW-21 concept vehicle are always equal to the maximum tractive force that can be generated and a model is developed for the tractive force using a track/seafloor peak friction coefficient and the track/seafloor rolling resistance coefficient, which are assumed to be constant throughout the transition. However, experience gained during

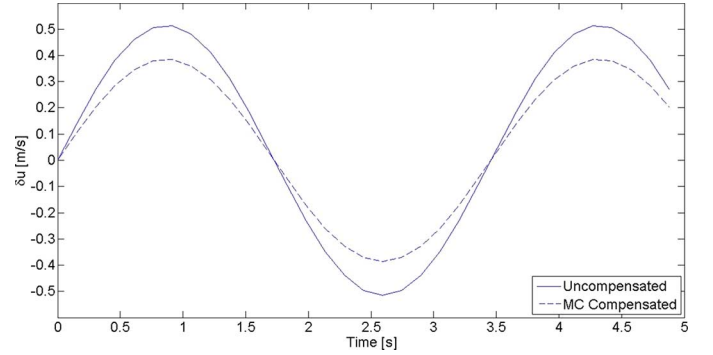


Fig. 41. Predicted surge velocity fluctuations caused by wave forces.

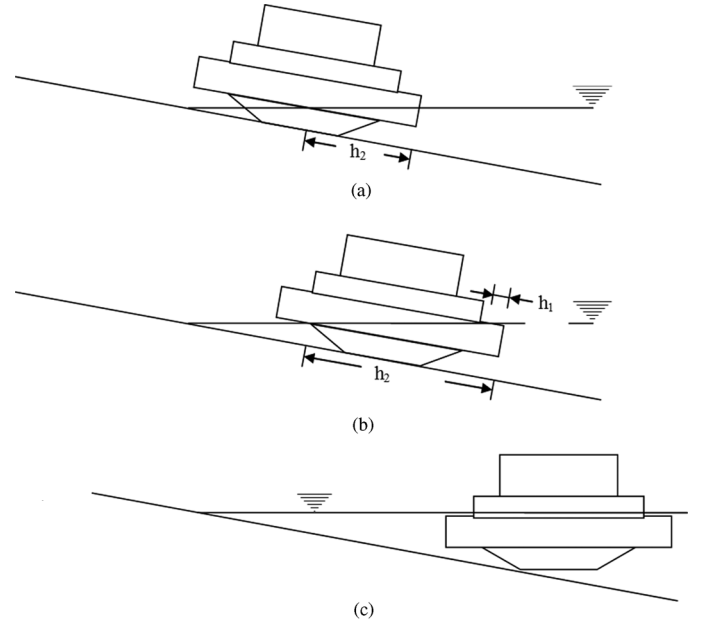


Fig. 42. Three cases for calculating volume of submerged SWATH hulls: (a) tops of SWATH hulls emerged; (b) tops of SWATH hulls immersed; and (c) buoyancy of submerged hulls completely supports vehicle weight.

initial testing of the DUKW-Ling scale model has shown that the track slip and, hence, the frictional coefficients vary through the transition zone.

Here, track slip i is defined as

$$i \equiv \frac{v_t - v_r}{v_t} \quad (15)$$

where v_t is the velocity of the track and v_r is the forward speed of the vehicle; note that the slip can be either positive or negative depending on whether the tangential speed of the track is faster or slower than the speed of the vehicle. Assuming uniform normal pressure on the tracks, the total tractive force developed by a tracked vehicle with slip on dry land is given by

$$H = (Ac + W \tan \phi) \left[1 - \frac{k}{il} \left(1 - e^{-il/k} \right) \right] \quad (16)$$

where $A = 2bl$ is the total contact area of the tracks, c is the cohesion, W is the weight of the vehicle, ϕ is the angle of internal

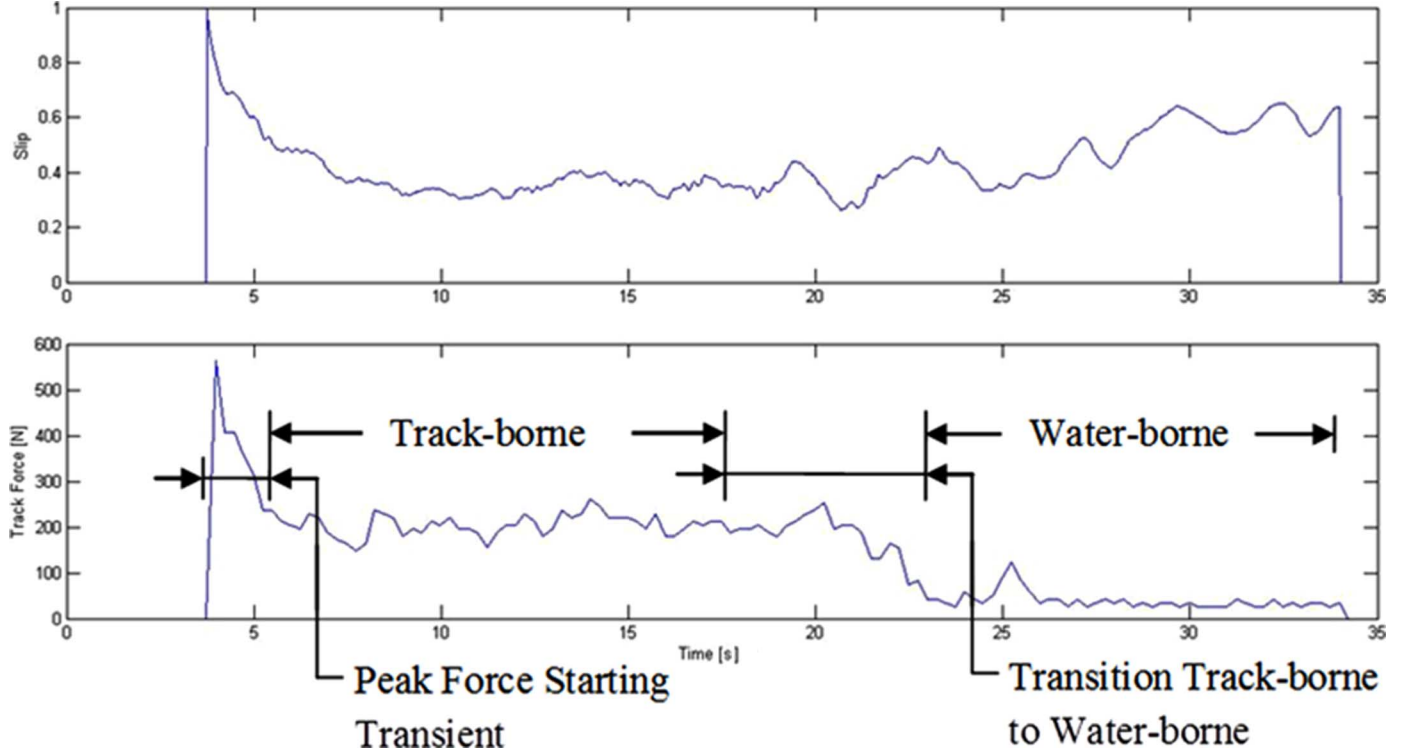


Fig. 43. Track slip and corresponding track force for land-to-sea transition test in Fig. 34. Track slip does not increase to $i = 1$ when the vehicle becomes waterborne because a combination of the vehicle's forward momentum and the slight thrust generated by the spinning tracks prevent the surge speed from dropping to $v_r = 0$.

shearing resistance of the soil, and k is the soil's shear deformation modulus [15]. Here, we modify the expression

$$H = \text{sgn}(i) (Ac + W_e \tan \phi) \left[1 - \frac{k}{|i|l} \left(1 - e^{-|i|l/k} \right) \right] \quad (17)$$

using the sign (signum) function $\text{sgn}(i)$ ¹ and absolute value of slip $|i|$, so that the tractive force can be calculated in situations where wave forces in the transition zone might be pushing the vehicle faster than it would be normally propelled by the tracks, and using an effective weight W_e , which accounts for the slope of the incline and the reduction in normal force with the ground owing to the increase in submerged hull volume ∇ as the vehicle enters the water

$$W_e = (\Delta - \rho g \nabla) \cos \theta. \quad (18)$$

Note that here Δ is the displacement of the vehicle, as in Table I.

Let h_2 be the longitudinal distance along the bottom of the submerged part of the hulls. Modeling the SWATH hulls as right circular cylinders, the submerged volume can be calculated as follows.

- 1) If $h_2 < 2r/\tan \theta$, where r is the radius of the SWATH hull and θ is the slope of the beach, the tops of the SWATH

¹The signum function of a real number x is defined as

$$\text{sgn}(x) = \begin{cases} -1, & x < 0 \\ 0, & x = 0 \\ 1, & x > 0 \end{cases}$$

hulls are completely above water [Fig. 42(a)]. Then, the displacement of each hull ∇_h is given by

$$\nabla_h = 2 \int_{r-\beta}^r \frac{h_2 (\xi - r + \beta)}{\beta} \sqrt{r^2 - \xi^2} d\xi \quad (19)$$

where $\beta = h_2 \tan \theta$ and the total submerged volume of both hulls is $\nabla = 2\nabla_h$.

- 2) When $h_2 \geq 2r/\tan \theta$, the tops of the SWATH hulls are partially submerged [Fig. 42(b)] and the submerged volume of each hull is given by $\nabla_h = (1/2)(h_1 + h_2) \pi r^2$, where h_1 is the submerged distance along the top of each hull in the longitudinal direction: $h_1 = h_2 - 2r/\tan \theta$. Then

$$\nabla_h = \left(h_2 - \frac{r}{\tan \theta} \right) \pi r^2 \quad (20)$$

where again $\nabla = 2\nabla_h$.

- 3) When the tracks are no longer in contact with the ground and the vehicle is completely supported by the buoyancy of the hulls [Fig. 42(c)] $\nabla = \Delta/(\rho g)$ and the effective weight is $W_e = 0$.

The motors used to turn the tracks are driven by closed-loop motor controllers that are programmed to maintain a constant track speed; the ability of the motors to maintain a set speed with varying output torque was confirmed in the dynamometer tests presented in Section III-A1a. The slip is calculated using the difference between the commanded velocity and measured DGPS data, as shown in Fig. 43.

Integrating the DGPS velocity measurements, the forward distance traveled by the vehicle as it moves through the surf-

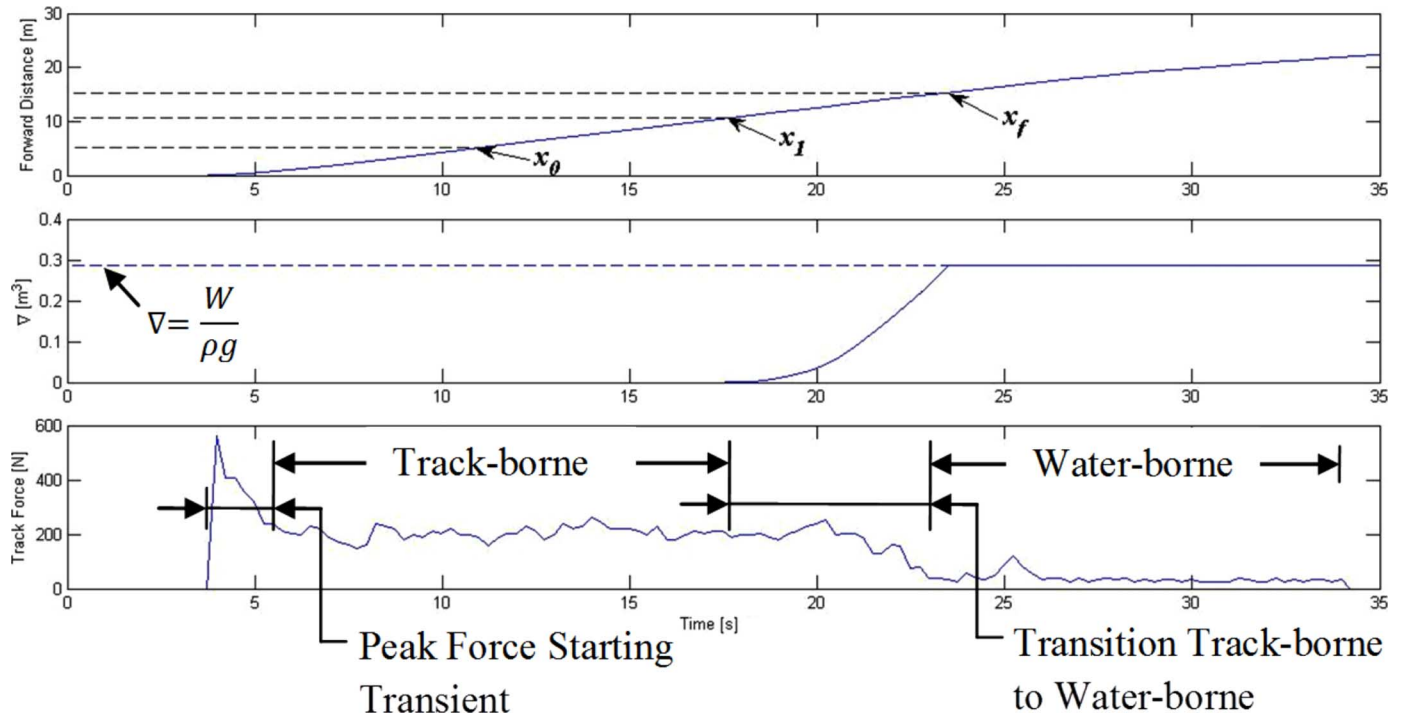


Fig. 44. Estimated position and submerged volume and effective weight of the vehicle in the surfzone. x_0 , x_1 , and x_f are the distances the vehicle travels before: the tracks make contact with the water (cross the mean beach waterline), the bow first enters the water, and the tracks leave the sand, respectively.

TABLE XII
COHESION c AND THE ANGLE OF INTERNAL SHEARING
RESISTANCE OF THE SOIL ϕ [15]

Terrain	Moisture Content [%]	c [kPa]	ϕ [°]
Rubicon sandy loam	43	3.7	29.8
Sandy loam (Hanamoto)	31	5.17	11.0
Sandy loam (Land Locomotion Lab)	15	1.72	29.0
Sandy loam (Land Locomotion Lab)	22	1.38	38.0
Dry sand (Land Locomotion Lab)	0	1.04	28.0

zone is calculated. Based on the estimated position of the vehicle with respect to the waterline, the submerged volume and effective weight of the vehicle are then determined (Fig. 44).

Using the estimated displacement, the effective weight of the vehicle was used in the modified form of Wong's tractive force model (17) to calculate the estimated track forces. In these calculations, empirical data for the cohesion c and the angle of internal shearing resistance of the soil ϕ for sandy soils with high moisture content, as well as dry sand, from [15] were used (Table XII). The soil's shear deformation modulus k typically ranges from 1 cm for firm sandy terrain to 2.5 cm for loose sand.

Use of these empirical values in the modified tractive force expression, across the entire range of k values possible, overpredicts the measured tractive forces by about 200%–300%. As the equipment required to obtain accurate measurements of the properties of the sand at the test site was not available, it was decided to explore the use of a least squares fit to provide estimates for the correct values of k , ϕ , and c to use in the tractive force model. The measured track forces from the motor controllers were Kalman filtered to reduce sensor and terrain noise before fitting. As shown in Table XIII, the fitted values of cohesion are about an order of magnitude smaller than the empirically determined values; additionally, the angle of internal shearing resis-

tance and the shear deformation modulus both increase as the value of the motor commands increase, and thus as the amount of slip present on the tracks increases. The corresponding estimated track forces are shown in Fig. 45(a)–(c). Note that although the process illustrates the possibility of determining empirical fits to the data for the purposes of modeling, the terrain values fit in Table XIII are not unique. Appropriate instrumentation should be used at field sites to determine the values experimentally, when possible. An additional assumption made in the application of this model is that the vehicle is moving along the direction of the maximum gradient of the slope of the beach, such that the force on each track is the same. A vehicle moving in a direction across the maximum gradient would experience a different normal force on each track owing to the roll moment created and could produce a curved trajectory [6].

VIII. CONCLUDING REMARKS

In this paper, we present the results of experimental testing of an unmanned tracked amphibious vehicle on dry sand, in the surfzone, and in water. The tests were performed to explore the vehicle's maneuvering and performance characteristics for the future development of an automatic control system. System identification of the data recorded from the flat ground and waterborne maneuvering trials was used to find linear parametric state-space models for the vehicle that adequately reproduces its motion in zigzag tests. The land-to-sea transition experiments show that the vehicle exhibits substantial track slip as it traverses the surfzone and its weight becomes increasingly supported by the displacement of its hulls. We also performed Froude–Krylov strip theory simulations and found that the wave forces acting on the vehicle in 28-cm waves are about the same magnitude as the force on each track and should not be ignored

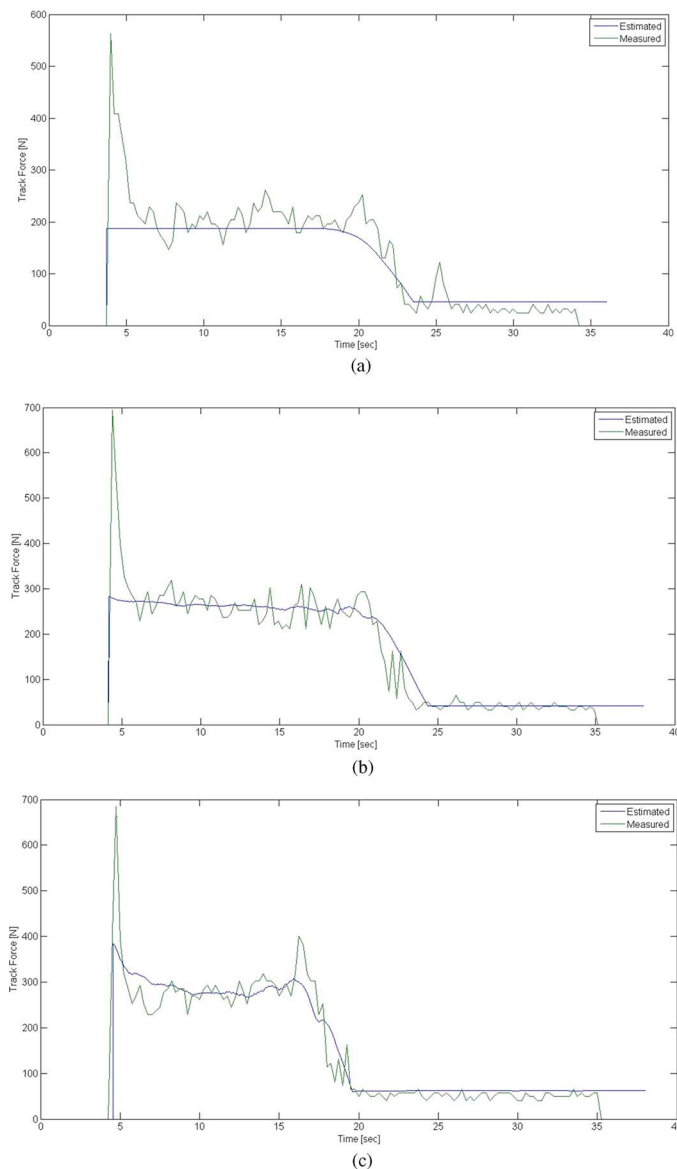


Fig. 45. Tractive effort measurements and predictions using terrain parameters determined from least squares curve fits. Tests were conducted at a significant waveheight of $H_{1/3} = 28$ cm and motor commands of (a) 64%, (b) 72%, and (c) 80% of maximum input.

TABLE XIII
TERRAIN VALUES FROM LEAST SQUARES FIT TO EXPERIMENTAL DATA

Motor Command [%]	c [kPa]	ϕ [°]	k [cm]
64	0.18	5.58	0.0
72	0.15	9.93	5.3
80	0.11	15.0	18

in modeling and simulation studies of the transition between land and sea. We modified the tractive force model developed by Wong for ground vehicles [15] to account for the buoyancy provided by the hull of an amphibious vehicle. The modified model captures the main physical features of the track forces measured during our transition experiments. However, the model utilizes three parameters that depend on soil properties (shear deformation modulus, angle of internal shearing resistance, and cohesion), and it overpredicts the measured track forces when using

values corresponding to dry sand and sandy loam; the soil at the test site consisted of wet and partially liquefied coarse sand. More accurate predictions may be possible if data are available for the soil at a particular vehicle deployment site.

Considering future work, it can be seen that, in general, the wave field, slope, bottom topography, and sediment properties that an amphibious vehicle might encounter in trying to make a transition from sea to land or land to sea would be difficult to predict *a priori*. Thus, from an automatic control perspective, both the plant parameters and disturbances acting on the system have a high degree of uncertainty and the use of a robust integral sliding mode controller [10], [14] or a model reference adaptive controller for such a vehicle would be an interesting direction of investigation. Additionally, the propulsion system is bimodal and strategies for most effectively utilizing either the tracks or the propellers, or some combination of the two, during the transition would complement the present study.

From a design standpoint, it would be useful to understand how the results of model testing might be scaled to predict the performance of a full-scale vehicle, particularly for the motion of the vehicle in the transition zone. Additionally, the sea-keeping properties of the vehicle's SWATH configuration make it a potentially useful unmanned surface vehicle platform for bathymetric survey applications [9] or environmental survey [11]. The wide hull spacing and high superstructure (perhaps coupled with some sort of buoyancy compensation device) may also make it well suited for the autonomous launch and recovery of unmanned underwater vehicles or for laying underwater cables from shore to sea, and future exploration of these applications is of interest.

REFERENCES

- [1] *Guide for Vessel Maneuverability*. Houston, TX, USA: American Bureau of Shipping, 2006, pp. 25–30.
- [2] O. Benoit, P. Gotteland, and A. Quibel, "Prediction of trafficability for a tracked vehicle on broken soil: Real size tests," *J. Terramechanics*, vol. 40, pp. 135–160, 2003.
- [3] C. A. Blackmon, B. G. Stinson, and J. K. Stoll, "An analytical model for predicting cross-country vehicle performance appendix D: Performance of amphibious vehicles in the water-land interface (hydrologic geometry)," U.S. Waterways Experiment Station, Tech. Rep. 3-783, 1970.
- [4] O. M. Faltinsen, *Hydrodynamics of High Speed Marine Vehicles*. New York, NY, USA: Cambridge Univ. Press, 2005, pp. 91–96, 236–237.
- [5] B. Flom, "DUKW-21 autonomous navigation: Autonomous path planning for an amphibious vehicle," Naval Surface Warfare Center, Carderock Division, West Bethesda, MD, USA, NSWCDD-CISD-2009/008 Ship Systems Integration & Design Dept. Tech. Rep., 2009.
- [6] B. Flom, "DUKW-21 autonomous navigation: Transitioning between sea and land," Naval Surface Warfare Center, Carderock Division, West Bethesda, MD, USA, NSWCDD-CISD-2010/015 Ship Systems Integration & Design Dept. Tech. Rep., 2010.
- [7] J. Finch, "AAAV design. Advanced amphibious assault vehicle final report Vol. 1," General Dynamics Amphibious Systems, Woodbridge, VA, USA, Annu. Rep., 2003.
- [8] F. Gonzales, R. Orme, A. Ruppert, and J. Schaffer, "DUKW 21—Amphibious cargo transfer from ship to shore," Naval Surface Warfare Center, Carderock Division, West Bethesda, MD, USA, NSWCDD-CISD-2007/01 Ship Systems Integration & Design Dept. Tech. Rep., 2007.
- [9] C. Kitts, P. Mahacek, T. Adamek, K. Rasal, V. Howard, S. Li, A. Badaoui, W. Kirkwood, G. Wheat, and S. Hulme, "Field operation of a robotic small waterplane area twin hull boat for shallow-water bathymetric characterization," *J. Field Robot.*, vol. 29, no. 6, pp. 924–938, 2012.

- [10] S. Laghrouche, F. Plestan, and A. Glumineau, "Higher order sliding mode control based on integral sliding mode," *Automatica*, vol. 43, no. 3, pp. 531–537, 2007.
- [11] J. Majohr, T. Buch, and C. Korte, "Navigation and automatic control of the Measuring Dolphin (MESSIN)," in *Proc. 5th IFAC Conf. Maneuv. Control Mar. Craft*, Aalborg, Denmark, 2000, pp. 405–410.
- [12] J. Marquardt, "Development and experimental testing of an amphibious vehicle," M.S. thesis, Dept. Ocean Mech. Eng., Florida Atlantic Univ., Dania Beach, FL, USA, 2012.
- [13] M. Quintero, "Model testing of ship dynamics in the surf zone," M.S. thesis, Dept. Ocean Resources Eng., Univ. Hawaii, Manoa, HI, USA, 2009.
- [14] V. Utkin, J. Guldner, and J. Shi, *Sliding Mode Control in Electro-Mechanical System*, 2nd ed. Boca Raton, FL, USA: CRC Press, 2009, ch. 7.
- [15] J. Y. Wong, *Theory of Ground Vehicles*, 3rd ed. New York, NY, USA: Wiley, 2001, ch. 2.
- [16] M. Young, "Design and analysis of an ocean current turbine performance assessment system," M.S. thesis, Dept. Ocean Mech. Eng., Florida Atlantic Univ., Dania Beach, FL, USA, 2012.



Joseph G. Marquardt received the B.S. and M.S. degrees in ocean engineering from Florida Atlantic University, Boca Raton, FL, USA, in 2010 and 2012, respectively.

He participated in the Naval Research Enterprise Internship Program in 2010 with the Center for Innovation in Ship Design at Naval Surface Warfare Center Carderock Division, and is currently a Research Assistant at Florida Atlantic University's Seatech Institute for Ocean and Systems Engineering, Dania Beach, FL, USA.

Mr. Marquardt is a Member of the Society for Naval Architects and Marine Engineers and the Tau Beta Pi Engineering Honors Society.



Jose Alvarez received the B.S. degree in ocean engineering from Florida Atlantic University, Boca Raton, FL, USA, in 2011.

He is currently a Research Assistant at the Florida Atlantic University's Seatech Institute for Ocean and Systems Engineering, Dania Beach, FL, USA. His areas of interest include towed systems, remotely operated vehicle (ROV) systems, buoy systems and subsea system installations.

Mr. Alvarez is a Member of the Society for Naval Architects and Marine Engineers.



Karl D. von Ellenrieder (M'08) received the B.S. degree in aeronautics and astronautics from the Massachusetts Institute of Technology (MIT), Cambridge, MA, USA, in 1990 and the M.S. and Ph.D. degrees in aeronautics and astronautics from Stanford University, Stanford, CA, USA, in 1992 and 1998, respectively.

He is currently an Associate Professor in the Department of Ocean & Mechanical Engineering, Florida Atlantic University, Dania Beach, FL, USA.

His research interests include marine hydrodynamics, ship design, and the development of unmanned surface vehicles. He participated in the ONR–ASEE Summer Faculty Fellowship Program with the Center for Innovation in Ship Design at Naval Surface Warfare Center Carderock Division in 2011 and 2012.

Prof. von Ellenrieder is a Member of the Society of Naval Architects and Marine Engineers, the Marine Technology Society, and the IEEE Oceanic Engineering Society.